

Development of HPC Based Phase Field Simulations Tool for Modification of Alloy Morphology to Enhance Material Properties during Additive Manufacturing (AM) Process



Balasubramaniam Radhakrishnan
Tahany El-Wardany
Ranadip Acharya

February 2023



DOCUMENT AVAILABILITY

Reports produced after January 1, 1996, are generally available free via OSTI.GOV.

Website www.osti.gov

Reports produced before January 1, 1996, may be purchased by members of the public from the following source:

National Technical Information Service
5285 Port Royal Road
Springfield, VA 22161
Telephone 703-605-6000 (1-800-553-6847)
TDD 703-487-4639
Fax 703-605-6900
E-mail info@ntis.gov
Website <http://classic.ntis.gov/>

Reports are available to US Department of Energy (DOE) employees, DOE contractors, Energy Technology Data Exchange representatives, and International Nuclear Information System representatives from the following source:

Office of Scientific and Technical Information
PO Box 62
Oak Ridge, TN 37831
Telephone 865-576-8401
Fax 865-576-5728
E-mail reports@osti.gov
Website <https://www.osti.gov/>

This report was prepared as an account of work sponsored by an agency of the United States Government. Neither the United States Government nor any agency thereof, nor any of their employees, makes any warranty, express or implied, or assumes any legal liability or responsibility for the accuracy, completeness, or usefulness of any information, apparatus, product, or process disclosed, or represents that its use would not infringe privately owned rights. Reference herein to any specific commercial product, process, or service by trade name, trademark, manufacturer, or otherwise, does not necessarily constitute or imply its endorsement, recommendation, or favoring by the United States Government or any agency thereof. The views and opinions of authors expressed herein do not necessarily state or reflect those of the United States Government or any agency thereof.

High Performance Computing for Energy Innovation (HPC4EI) Report

**DEVELOPMENT OF HPC BASED PHASE FIELD SIMULATIONS TOOL FOR
MODIFICATION OF ALLOY MORPHOLOGY TO ENHANCE MATERIAL
PROPERTIES DURING ADDITIVE MANUFACTURING (AM) PROCESS**

Balasubramaniam Radhakrishnan
Computational Sciences and Engineering Division, Oak Ridge National Laboratory

Tahany El-Wardany, Raytheon Technologies Research Center
Ranadip Acharya, Collins Aerospace Applied Research and Technology

February 2023

Prepared by
OAK RIDGE NATIONAL LABORATORY
Oak Ridge, TN 37831
managed by
UT-BATTELLE LLC
for the
US DEPARTMENT OF ENERGY
under contract DE-AC05-00OR22725

CONTENTS

CONTENTS	iii
LIST OF FIGURES	4
LIST OF TABLES	5
ABSTRACT.....	6
1. INTRODUCTION	7
1.1 Background	7
1.2 Problem Description	8
1.3 Approach.....	8
1.4 motivation	9
2. STATEMENT OF OBJECTIVES	9
3. BENEFITS TO THE FUNDING DOE OFFICE'S MISSION	10
4. RESULTS	10
4.1 Heat Transfer Modeling of AM Process AT RTRC	10
4.1.1 Gibbs Energies of phases	11
4.1.2 Thermodynamically Consistent Nucleation Model for CET	13
4.1.3 Implementation of the nucleation model	14
4.2 demonstration of the PF CET simulations for Ti-Cu alloy	15
4.3 Application of Validated Phase Field Model to Ti-Cu AM geometries	18
4.3.1 Effect of G and R on CET.....	18
4.3.2 Effect of Cu content on CET in Ti-Cu Alloys	20
4.3.3 Effect of Time Varying G and R on CET	24
4.4 CET simulations in Ti-Nb-Cu ternary alloys.....	26
4.4.1 Summary Discussion of phase field simulations of CET	33
4.5 AM experiments and CHARACTERIZATION at RTRC	35
4.5.1 Chemical Compositions	37
4.5.2 Microstructures	37
4.5.3 Mechanical Testing.....	39
4.5.4 Summary of Experimental Results	40
5. REFERENCES	40
ACKNOWLEDGMENTS	42

LIST OF FIGURES

Figure 1. Large, elongated grains in the build direction for Ti-6Al-4V (left) and fine, equiaxed grains for Ti-8.5 wt.% Cu alloy (right) obtained during DED [7].	8
Figure 2. Overall project plan integrating computational tasks proposed in this project with the experimental effort at RTRC.	9
Figure 3. Solidification rate, $R(t)$, (left) and temperature gradient, $G(t)$, in the liquid (right) as a function of solidification time along centerline of the melt pool extracted from the heat transfer simulations.	12
Figure 4. Ti-rich end of the Ti-Cu phase diagram obtained using ThermoCalc CALPHAD functions.	14
Figure 5. Bulk nucleation and evolution of CET during solidification of a Ti-0.06Cu alloy using PF parameters shown in Table 1. Copper concentration contours are shown after various solidification times.	17
Figure 6. Grain orientation angles of the evolving nuclei shown in Figure 5 above.	17
Figure 7. Increase in CET grain size due to decreasing nucleation density introduced by changing the nucleation parameter. The grain size is larger than in Figures 5 and 6.	18
Figure 8. Temporal evolution of CET in Ti-0.06Cu alloy using $G = 348132$ K/m and $R = 0.029$ m/s showing fully equiaxed microstructure.	20
Figure 9. Transition in the solidification microstructure from fully equiaxed to columnar grains with different orientations than in the substrate due to bulk nucleation in the liquid.	20
Figure 10. Titanium-rich end of the Ti-Cu phase diagram calculated using SSOL4 database in ThermoCalc. The three Ti-Cu alloys used in the PF simulations.	21
Figure 11. Simulated solidification microstructure for Ti-0.03Cu showing the dendrite orientations (left) and the Cu concentration field (right).	22
Figure 12. Simulated CET microstructure during solidification of Ti-0.06Cu alloy showing dendrite orientations (left) and Cu concentration field (right).	22
Figure 13. Simulated CET microstructure during solidification of Ti-0.08Cu alloy showing dendrite orientations (left) and Cu concentration field (right).	23
Figure 14. Temporal evolution of solidification height and s-l interface velocity, V (left) and s-l interface temperature (right). The constant imposed solidification rate (pulling velocity) is marked in the figures.	23
Figure 15. Spatial temperature distribution during solidification of Ti-0.03Cu (left), Ti-0.06Cu (middle) and Ti-0.08Cu (right) showing the undercooling in the liquid ahead of the epitaxial front.	24
Figure 16. Magnified sections of Figures 11-13, showing the dendritic structure along the vertical line used for calculating the local liquidus temperatures. Left – 0.03Cu, Middle – 0.06Cu and Right – 0.08Cu.	25
Figure 17. Cu concentration profile at the start of the nucleation (left) and structure after longer solidification time in Ti-06Cu solidified with variable G and R from Table 2.	25
Figure 18. Interface velocity (V) (right) and dendrite tip temperature (left) as a function of solidification time for the solidification condition shown in Figure 17.	26
Figure 19. Effect of heterogeneous nucleation parameters on the morphology of CET grains.	27
Figure 20. Bulk nucleation in the liquid for Ti-0.2Nb-0.06Cu alloy for $V = 0.029$ m/s for various G values.	28
Figure 21. Bulk nucleation in the liquid for Ti-0.2Nb-0.06Cu alloy for $V = 0.05$ m/s at various G values.	28
Figure 22. Bulk nucleation in the liquid for Ti-0.2Nb-0.06Cu alloy for $V = 0.08$ m/s at various G values.	29
Figure 23. Bulk nucleation in the liquid for Ti-1e-5Nb-0.06Cu alloy for $V = 0.01$ m/s at various G values.	29
Figure 24. Bulk nucleation in the liquid for Ti-1e-5Nb-0.06Cu alloy for $V = 0.05$ m/s at various G values.	30
Figure 25. Bulk nucleation in the liquid for Ti-1e-5Nb-0.06Cu alloy for $V = 0.08$ m/s at various G values.	31
Figure 26. Temporal evolution of the solidification microstructure for Ti-1.e-5Nb-0.06Cu alloy showing liquid nucleation and the formation of equiaxed grains.	32
Figure 27. Solidification microstructure of Ti-0.1Nb-0.06Cu (left) and microstructure at the beginning of nucleation for Ti-0.2Nb-0.06Cu (right).	32
Figure 28. Effect of nucleation parameters on bulk nucleation in Ti-1e-5Nb-0.06Cu alloys.	33
Figure 29. Effect of nucleation parameters on bulk nucleation Ti-0.2Nb-0.06Cu alloy.	33
Figure 30. Portion of the Ti/Cu phase diagram [19] indicating the selected compositions for L-DED.	36

Figure 31. Optical images of the cross-section of raw powders. Blue is image of the titanium powder and green is image of copper powder. The powders are spherical, between 45 μm to 105 μm in diameter.	37
Figure 32. BSE images. a and b are BSE images of as-printed specimens showing the fine α phases when multiple layers were deposited, for Ti–3.5Cu (a) and Ti–6.5Cu (b) [3]; c and d results are obtained using DED at RTRC. When the copper content in the alloy is 3-4% the grain structure produced is the same as in a and b , however with the increase in the copper content grain refinement occurs not across all the layers, but only in the first and last layers.	39
Figure 33. Transmission electron microscopy characterization of as-printed Ti–6.7Cu alloy. a, Bright-field image showing the eutectoid lamellar structure. b–d, X-ray energy dispersive spectroscopy (XEDS) mapping on a section of the eutectoid lamellar structure: Oxygen elemental map (b), titanium elemental map (c) and copper elemental map (d). XEDS point analyses show that the copper contents in the lamellar structure are 3.3 wt% in α -phase titanium.	40

LIST OF TABLES

Table 1. PF parameters used in the initial CET investigations	14
Table 2. Time dependent G and R as a function of solidification time of melt pool.....	17
Table 3. Nucleation parameters used in the parametric study	34

ABSTRACT

Currently, additive manufacturing (AM) technology is extensively used to manufacture aerospace components because of the unique advantages of the technique in producing custom designs, complex geometries in a near-net fashion that significantly reduces the manufacturing cost, and improved energy efficiency. However, the thermodynamic properties of existing aerospace alloys and the thermal conditions that prevail in most of the powder-bed based additive manufacturing processes lead to undesirable columnar / columnar-dendritic microstructures that promote solidification cracking during the process, and the development of anisotropy in the mechanical properties of the as-built components. Time consuming, energy-intensive post AM treatments are required to recover the mechanical properties of the wrought components for which the existing alloy compositions were designed for. However, novel alloy compositions, that exploit the AM thermal conditions to produce fine, equiaxed grain structures in the as-built condition, with mechanical properties equal to or exceeding those of the wrought work-horse alloy, Ti-6Al-4V has recently been demonstrated in Ti-Cu alloys. Significant energy savings up to 66% can be obtained for a typical aerospace component through digitally designing the AM process, process parameters, and alloy composition. The current project focused on developing a fundamental understanding of the evolution of the columnar to equiaxed transition (CET) occurring during solidification under AM thermal conditions in Ti-Cu and Ti-Cu-X alloys using high-fidelity phase field (PF) simulations using the leadership class computing facilities that exist in the national laboratories. The simulations were able to capture the effect of alloy and process conditions on CET, and clearly showed the beneficial effect of a ternary solute addition to Ti-Cu binary alloys on CET. The simulations indicated that bulk nucleation in the liquid ahead of the solidifying epitaxial front was promoted by a large, transient, thermal undercooling promoted by the mismatch between the growth rate of the dendrite tips in the epitaxial front and the imposed solidification rate. AM experiments performed at Raytheon Technologies Research Center using the same thermal conditions used in the PF simulations indicated the formation of equiaxed grains, although the grain size was bigger than the ones reported in the literature. On the other hand, the equiaxed grain size predicted by PF simulations were smaller than the grain size of Ti-Cu alloys reported in the literature. The industry will follow up the existing work in a future program that would involve further optimization of the process for the Ti-Cu-X alloys to demonstrate the application of the process and the alloy to a specific aerospace component.

1. INTRODUCTION

1.1 BACKGROUND

Currently many (alpha-beta, beta, and metastable beta) titanium alloys used in the aerospace industry are produced by conventional processes such as casting, and by thermo-mechanical processing such as rolling, forging, extrusion, etc. Additive manufacturing (AM) offers a unique advantage in making near-net-shape components of complex geometry in metallic alloys resulting in significant cost and energy savings. However, a potential challenge is to meet the demanding mechanical property requirements in these components owing to constraints involved in fusion-based AM processes, as well as the common practice of trying to use the same wrought alloy compositions for AM processing where the material experiences a vastly different thermal history than in conventional processes for which they are optimized.

The most common, work horse, titanium alloy used by the aerospace industry is the wrought alloy Ti-6 wt.%Al-4wt.%V. The same alloy composition has often been used to manufacture components using fusion based AM processes. However, the microstructure in the AM component almost always tends to be columnar in nature, with the columns aligned along the build direction. Such an arrangement leads to anisotropy in mechanical properties between the build direction and transverse to the build direction, which is undesirable. However, it is known that replacing the columnar grains with fine equiaxed grains during solidification is beneficial both for reducing the hot cracking tendency during AM processing [1] as well as for achieving isotropic mechanical properties in the as-built condition. The occurrence of columnar to equiaxed transition (CET) during AM solidification of Ti-6Al-4V can be explained on the basis of a low growth restriction factor, Q defined as $C_0 m(1-k)$ where C_0 is the average alloy composition, m is the liquidus slope, and k is the partition coefficient of the solute defined as C_s/C_l [2]. The main reason for the low Q value in Ti-6Al-4V is the poor partitioning of the Al and V solutes into the liquid that results in negligible constitutional supercooling (CS) in the liquid. Based on theories of alloy solidification, in order to achieve CET at low Q values, it is required to maintain a very low value of G/R in the liquid, where G is the temperature gradient in the liquid, and R is the externally imposed solidification rate. Such a thermal condition is very difficult to achieve in conventional powder-bed based AM processes using laser or electron beams.

There have been several attempts to achieve CET in Ti-6Al-4V during AM by manipulating energy input per unit volume, wire-based AM processes [3], beam shaping [4], and the introduction of ultrasonic vibration [5], or inoculant particles [6] in the liquid in order to promote nucleation of solid in the supercooled liquid. While the approaches based on thermal management have been demonstrated for simple geometries, application to complex geometries in narrow-freezing alloys is very challenging. Since AM involves layer-by-layer build-up of a component, the layer geometry varies with changes in the local cross section in the AM component that leads to significant differences in the thermal conditions of the melt pool from one location to another. Approaches based on ultrasonic vibration are more promising provided the vibration parameters required to form the equiaxed grains at specific locations in a component with a complex geometry are known *a priori*.

A more practical solution to the utilization of AM to manufacture near-net-shape titanium alloy components is to design unique compositions that are highly prone to forming fine, equiaxed dendrites through CET under AM solidification conditions. Such an alloy design concept for AM has recently been demonstrated in a Ti-Cu binary alloy [7]. The as-processed microstructure obtained using laser powder bed fusion AM in a Ti-8.5%Cu alloy shows equiaxed grains roughly 10 μm in diameter [7]. The microstructures obtained in Ti-6Al-4V and Ti-8.5%Cu alloy obtained in [7] are shown in Figure 1.

The CET in Ti-Cu alloys was attributed to large Q values that results in extensive CS in the liquid. The large Q value also results in the extremely fine equiaxed grain size based on the interdependence theory

[2]. By comparing the phase diagrams of Ti-6Al-4V and a Ti-8.5 wt.% Cu alloy, it was shown that the Ti-Cu alloy had a Q value that was roughly eight times larger than that of Ti-6Al-4V. It was concluded that the undercooling required to nucleate the equiaxed grains, ΔT_n , was lower than the extent of undercooling in the CS zone, ΔT_{cs} , in Ti-Cu alloys while the condition was not satisfied for Ti-6Al-4V.

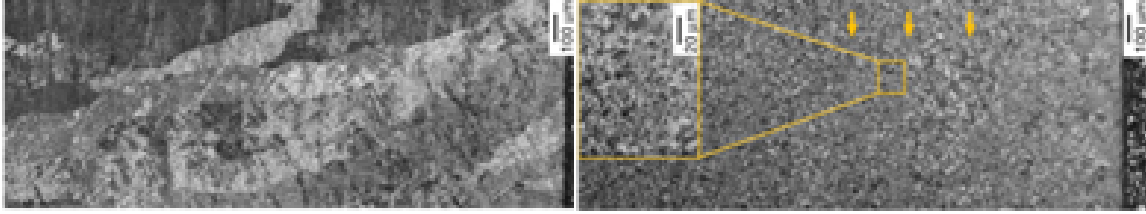


Figure 1. Large, elongated grains in the build direction for Ti-6Al-4V (left) and fine, equiaxed grains for Ti-8.5 wt.% Cu alloy (right) obtained during DED [7].

1.2 PROBLEM DESCRIPTION

The objective of this research is to develop a more fundamental understanding of the CET in Ti-Cu alloys solidifying under AM thermal conditions, including the transient solidification conditions that occur during AM, and the time-dependent thermal gradient in the liquid, $G(t)$, and the time-dependent solidification rate, $R(t)$, that occurs during the solidification of the AM melt pools using high performance computing (HPC) based phase field (PF) simulations. This knowledge will allow addressing the challenge of identifying alloys that can demonstrate CET over a wide range of thermal conditions given the complex geometry of the aerospace components. The simulations will be used to optimize potential Ti-Cu and Ti-Cu-X compositions that Raytheon Technologies Research Center (RTRC) will use in proof-of-principle experiments to test the validity of such a modeling-based approach to design AM titanium alloys.

1.3 APPROACH

Based on the demonstration of CET and the formation fine, equiaxed grains during direct energy deposition (DED) AM of Ti-Cu alloys in the literature [7], the computational tasks in this project were focused on utilizing PF simulations to explore the CET in binary Ti-Cu and Ti-Cu-X alloys under thermal conditions characteristic of DED. The thermal boundary conditions to drive the PF simulations were obtained from melt-pool level thermal simulations performed by RTRC. The existing HPC capability in PF modeling afforded by the Microstructure Evolution Using Massively Parallel Phase-field Simulations – Solid-Liquid (MEUMAPPS-SL) code [8] at the Oak Ridge National Laboratory (ORNL) was used in performing the PF simulations. An additional capability to include the nucleation of solid grains in the liquid pool ahead of the epitaxially solidifying front was developed and implemented in MEUMAPPS-SL. The computing facilities at Oak Ridge Leadership Computing Facility, and the HPC capabilities at the National Renewable Energy Laboratory (NREL) were used to run the MEUMAPPS-SL under HPC environment. The computing time at ORNL Summit supercomputer was obtained through an Argonne Leadership Computing Challenge award [9], and an additional allocation was obtained to utilize the supercomputer, Eagle, situated at NREL [10]. RTRC initiated an experimental effort to perform DED experiments in Ti-Cu using the approach used in the literature [7], to check the reproducibility of the experimental results of CET and the associated mechanical properties. The overall capability by combining PF simulations with experiments conducted at RTRC to develop novel Ti-Cu alloys is illustrated in Figure 2.

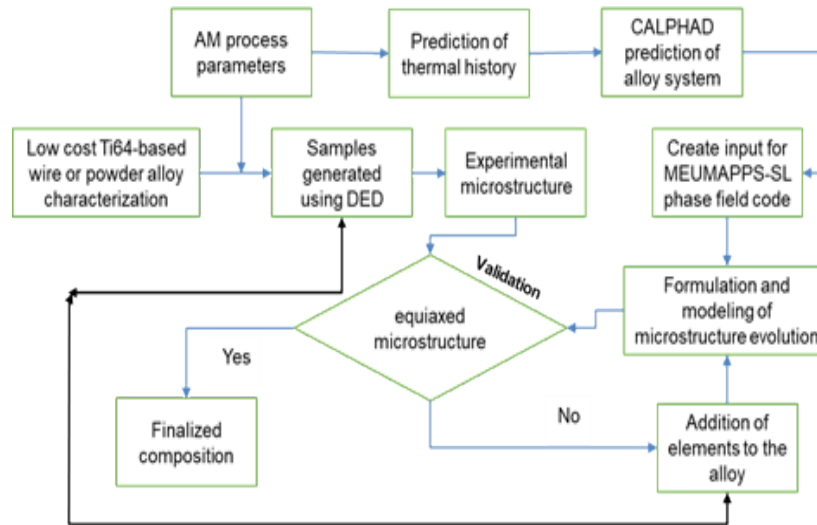


Figure 2. Overall project plan integrating computational tasks proposed in this project with the experimental effort at RTRC.

One of the challenges in simulating CET during solidification is the uncertainty in the factors that contribute to the nucleation of solid in the bulk liquid. The thermodynamically consistent nucleation model implemented in MEUMAPPS-SL reduced the uncertainty essentially to two parameters. Consequently, the approach was to systematically vary the two parameters to identify the set of conditions that would reproduce the CET microstructures obtained in [7] for Ti-Cu alloys. Once the parameters were fixed, the plan was to extend the simulations to other Ti-Cu and Ti-Cu-X compositions to investigate the effect of alloy composition on CET. The simulations were also extended to different constant sets of G and R as well as the time varying $G(t)$ and $R(t)$ in order to investigate the effect of thermal conditions on CET.

1.4 MOTIVATION

This project is motivated by the significant potential benefit to the aerospace industry due to the possibility of producing new alloys by exploiting the thermal conditions during AM to replace the more expensive wrought alloys. The potential to meet property requirements in the as-built condition could eliminate energy-intensive post-build heat treatments. In addition, the use of a near-net process such as AM to manufacture complex component geometries results in the minimization of machining operations. Based on the analysis performed by Raytheon, the overall energy savings in the production of an integrated blade rotor could be up to 66%.

2. STATEMENT OF OBJECTIVES

The technical objectives of this research are listed below.

- **Heat Transfer Modeling of AM process:** Perform melt-pool level thermal simulations of the DED AM process and provide time dependent temperature gradient (G), and solidification rate (R) at typical locations in the melt pool as input to the phase field simulations.
- **Development of Thermodynamic Input to Phase Field Simulations:** Obtain Gibbs free energies for the liquid and solid phases as a function of temperature for the Ti-Cu and Ti-Nb-Cu systems either through open Calculation of Phase Diagrams CALPHAD assessments or parameterized using ThermoCalc database.

- Validation of PF simulations for Ti-Cu alloy: Perform MEUMAPPS-SL simulations of CET in Ti-Cu base alloy using a set of G and R values corresponding to a specific location in the experimental build. Simulate the influence of the nucleation parameters on CET and the volume fraction of the eutectic liquid. Tune the nucleation parameters to match the experimentally determined microstructure at RTRC.
- Application of validated PF model to Ti-Cu AM geometries: Perform simulations to determine the robustness of the Ti-Cu alloy to equiaxed grain formation over the range of G and R conditions encountered during an AM build due to local changes in the cross section for a component with complex geometry.
- Application of PF simulations to Ti-Nb-Cu ternary alloys: Extend the simulations Ti-Nb-Cu ternary alloy to investigate the effect of ternary Nb addition on CET.
- AM experiments using Ti-Cu binary alloys: Perform AM experiments using powder DED process to support the phase field simulations.
- Characterization of AM materials for model validation and verification through optical and scanning electron microscopy and tensile tests.
- Model validation and refinement: Validate and refine phase field model based on experimental results.

3. BENEFITS TO THE FUNDING DOE OFFICE'S MISSION

ORNL is a major partner in the HPC for Manufacturing (HPC4Mfg) program. The work performed under this HPC4Mfg project is relevant to AM, which is one of the leading activities under the Advanced Manufacturing Office (AMO) of the DOE. The work focuses on utilizing HPC to predict CET during solidification of Ti based alloys under AM conditions to design new aerospace Ti alloys.

4. RESULTS

4.1 HEAT TRANSFER MODELING OF AM PROCESS AT RTRC

The primary focus of the modeling effort is the 3D estimation of the melt pool and mushy zone dimensions as well as melt pool temperature distribution. The temperature fields, and the local cooling rates were processed to extract the $G(t)$ and $R(t)$ that were used to drive the PF simulations. A finite-volume based heat transfer model was used to predict the melt pool dimension. Commercial software Analysis System for Computational Fluid Dynamics (ANSYS CFX) multiphase module was used with a species model for capturing the solid to liquid phase change and subsequent re-solidification. This essentially allowed capturing the bottom surface of the melt pool in addition to the prediction of melt pool width and depth. The heat transfer model was based on conduction only, and fluid flow effects are neglected. To account for the effect of solidified region adjacent to the melt pool, a Darcy-like momentum sink model was used. During the LPBF process, the laser heat source was focused on the powder-substrate interface to allow better wetting for the powder and to avoid balling. A volumetric heat source model was utilized to simulate the laser. Laser beam energy distribution was assumed to be a Gaussian bell in the scan (x), and transverse (y) directions, and with exponential decay in depth direction (z) for both powder layer and substrate depth. Also, the source term was modified to have maximum value at the powder-substrate interface. The laser parameters used for the current model corresponded to a power of 800W, with a scan velocity of 800 mm/min, a spot diameter of 1.5mm and an assumed an absorptivity of

0.55. The grid count for the conduction model was roughly 261,000 for a 125 mm x 6 mm x 2.5 mm domain. We used adaptive time stepping to solve the problem and limited maximum timestep to 1×10^{-4} s to have adequate resolution in time. The thermophysical input properties to the heat transfer model were obtained using the TCTI4 database in ThermoCalc. The solidification rate $R(t)$ and the temperature gradient $G(t)$ extracted from the cooling rates along the center line of the melt pool as a function of the solidification time are shown in Figure 1. These values were used in the subsequent PF simulations.

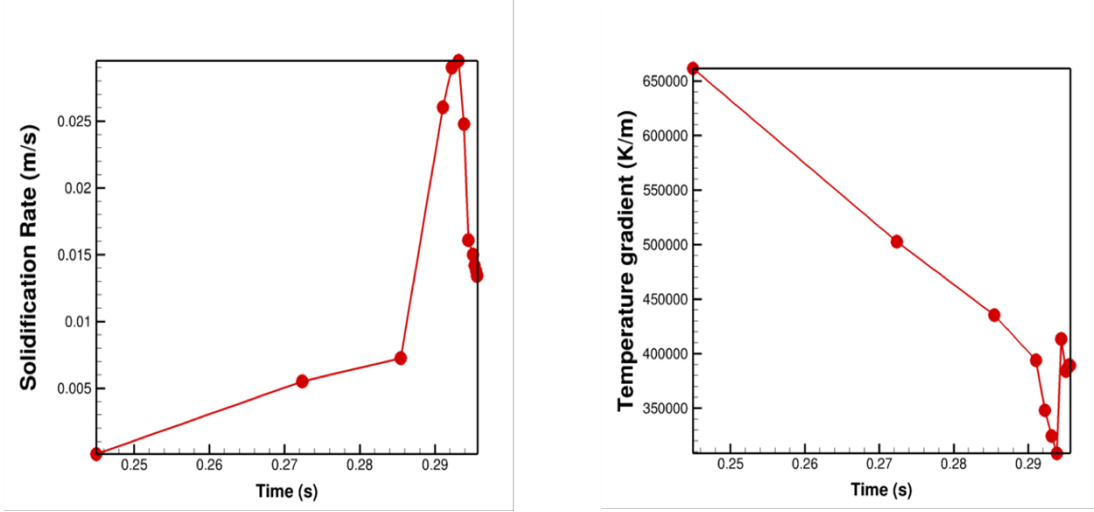


Figure 3. Solidification rate, $R(t)$, (left) and temperature gradient, $G(t)$, in the liquid (right) as a function of solidification time along centerline of the melt pool extracted from the heat transfer simulations.

4.1.1 Gibbs Energies of phases

The chemical free-energy densities (Gibbs energies of phases) are defined using the CALPHAD approach based on the Redlich-Kister polynomials [11] to describe the effect of solute interaction coefficients on the excess free energies of liquid and solid phases. Accordingly, the total free energy of mixing for a phase, p , for a binary alloy, G_m^p is given by,

$$G_m^p = c_A G_A^0 + c_B G_B^0 + RT\{c_A \ln c_A + c_B \ln c_B\} + c_A c_B \sum_{i=0}^{n_{AB}} L_{A,B;i} (c_A - c_B)^i \quad [1]$$

where the first two terms on the right-hand side represent the standard free energy of formation, the third term represents the ideal entropy of mixing, and the last term represents the excess energy defined using the binary interaction coefficients, $L_{A,B;i}$. For the Ti-Cu alloy used in the simulations, G_A^0 , G_B^0 , and $L_{A,B;i}$ were obtained from the SSOL4 database in ThermoCalc, as shown below. A Fortran routine calculated the local values of the free energies of the solid and liquid phases based on the local solid and liquid compositions [8]. The standard Gibbs energies of the liquid phases of Cu and Ti, respectively, are shown in Equations 2 and 3 below.

G(LIQUID,CU;0)-H298(FCC_A1,CU;0) =

$$298.15 < T < 1357.77: \quad 5194.277 + 120.973331T - 24.112392T \log(T) - 0.00265684T^2 + 1.29223E^{-07}T^3 + 52478T^{-1} - 5.8489E^{-21}T^7$$

$$1357.77 < T < 3200.00: \quad -46.545 + 173.881484T - 31.38T \log(T)$$

[2]

$$G(\text{LIQUID}, \text{Ti}; 0) - H_{298}(\text{HCP_A3}, \text{Ti}; 0) =$$

$$\begin{aligned} 298.15 < T < 900.00: & 4134.494 + 126.63427T - 23.9933T \log(T) - \\ & 0.004777975T^2 + 1.06716E-07T^3 + 72636T^{-1} \\ 900.00 < T < 1155.00: & 4382.601 + 126.00713T - 23.9887T \log(T) - 0.0042033T^2 - \\ & 9.0876E-08T^3 + 42680T^{-1} \\ 1155.00 < T < 1300.00: & 13103.253 + 59.9956T - 14.9466T \log(T) - 0.0081465T^2 + \\ & 2.02715E-07T^3 - 1477660T^{-1} \\ 1300.00 < T < 1941.00: & 369519.198 - 2554.0225T + 342.059267T \log(T) - \\ & 0.163409355T^2 + 1.2457117E-05T^3 - 67034516T^{-1} \\ 1941.00 < T < 4000.00: & -19887.066 + 298.7367T - 46.29T \log(T) \end{aligned} \quad [3]$$

The binary interaction coefficients between Ti and Cu, L0, L1 and L2 are shown in Equation 4.

$$\begin{aligned} L(\text{LIQUID}, \text{Cu}, \text{Ti}; 0) &= -19341.505 + 8.139934T \\ L(\text{LIQUID}, \text{Cu}, \text{Ti}; 1) &= 0.0 \\ L(\text{LIQUID}, \text{Cu}, \text{Ti}; 2) &= 9403.872 - 5.586502T \end{aligned} \quad [4]$$

The standard Gibbs energy of the primary solid phase BCC_A2 for Cu and Ti is given in Equations 5 and 6, respectively.

$$G(\text{BCC_A2}, \text{Cu}; \text{VA}; 0) - H_{298}(\text{FCC_A1}, \text{Cu}; 0) =$$

$$\begin{aligned} 298.15 < T < 1357.77: & -3753.458 + 129.230235T - 24.112392T \log(T) \\ & - 0.00265684T^2 + 1.29223E-07T^3 + 52478T^{-1} \\ 1357.77 < T < 3200.00: & -9525.026 + 182.548828T - 31.38T \log(T) + 3.64167E^{29}T^{-9} \end{aligned} \quad [5]$$

$$G(\text{BCC_A2}, \text{Ti}; \text{VA}; 0) - H_{298}(\text{HCP_A3}, \text{Ti}; 0) =$$

$$\begin{aligned} 298.15 < T < 1155.00: & -1272.064 + 134.71418T - 25.5768T \log(T) - 6.63845E-04T^{**2} - \\ & 2.78803E-07T^{**3} + 7208T^{**(-1)} \\ 1155.00 < T < 1941.00: & 6667.385 + 105.366379T - 22.3771T \log(T) + 0.00121707T^2 - \\ & 8.4534E-07T^3 - 2002750T^{-1} \\ 1941.00 < T < 4000.00: & 26483.26 - 182.426471T + 19.0900905T \log(T) - \\ & 0.02200832T^{**2} + 1.228863E-06T^{**3} + 1400501T^{**(-1)} \end{aligned} \quad [6]$$

The binary interaction coefficient between Ti and Cu for the BCC_A2 phase is given by

$$L(\text{BCC_A2}, \text{Cu}, \text{Ti}; \text{VA}; 0) = 4184.714 \quad [7]$$

The BCC-A2 phase an addition contribution from magnetic ordering below Curie temperature given by,

$$1 - .905299383\tau^{-1} - .153008346\tau^3 - .00680037095\tau^9 - .00153008346\tau^{15} \quad [8]$$

and above Curie Temperature given by

$$-0.0641731208\tau^{-5} - .00203724193\tau^{-15} - 4.27820805E-04\tau^{-25} \quad [9]$$

A key capability required to simulate CET is the development of a nucleation model that can capture the effect of alloy thermodynamics on the nucleation rate that can be easily implemented into MEUMAPPS-SL. A brief description of the nucleation model and its implementation in MEUMAPPS-SL are described

below. The implementation of a nucleation model in the liquid to simulate CET (to be discussed below) requires the solidus and liquidus temperatures of the liquid ahead of the solidifying epitaxial front. Figure 4 shows the solidus and liquidus curves for the Ti-Cu binary calculated using ThermoCalc and fitted to polynomial functions that are used in MEUMAPPS-SL. The data used to fit the solidus and liquidus in Figure 4 are only for Cu concentrations up to 0.25 mole fraction because of the expected solute enrichment in the liquid for the binary alloys based on the slopes of the solidus and liquidus lines, and the alloys of interest, Ti-0.035Cu, Ti-0.065Cu and Ti-0.08 Cu.

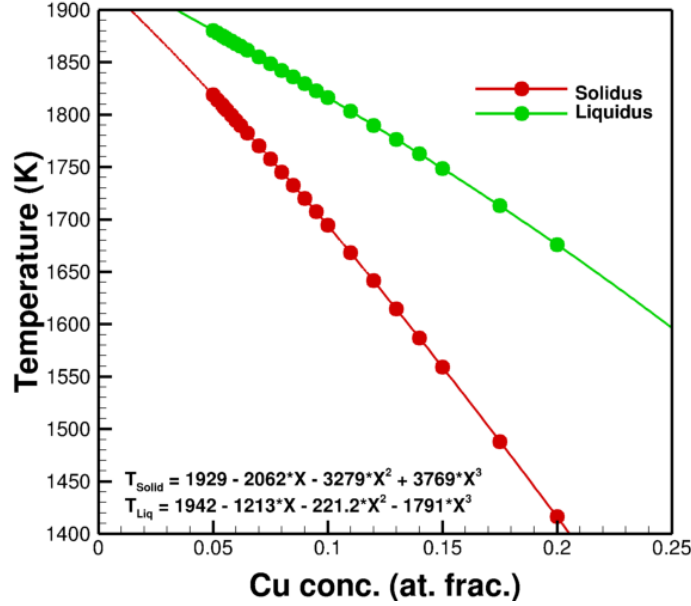


Figure 4. Ti-rich end of the Ti-Cu phase diagram obtained using ThermoCalc CALPHAD functions.

4.1.2 Thermodynamically Consistent Nucleation Model for CET

There have been attempts to replace the simple nucleation models used for nucleation of CET with models that are more thermodynamically consistent. A thermodynamic framework for calculating the composition, C_s , of a solid nucleus from solute enriched liquid of composition C_l was proposed by Spaepen and Thompson [12] based on the suggestion that C_s maximizes the resulting thermodynamic driving force per unit volume, ΔG_v . Their calculations show that under this assumption, the change in the chemical potentials of the solutes due to the phase change is the same, which leads to the following condition,

$$\frac{\partial G_l}{\partial C_l} = \frac{\partial G_s}{\partial C_s} \quad [10]$$

where G_l and G_s are the Gibbs free energies of the solid and liquid phases per unit volume. Incorporating the above value of ΔG_v theory, Li et al. [13] proposed the following equation based on the classical nucleation theory to describe the nucleation rate in the CS zone

$$I = I_0 \exp \left[-\frac{16\pi\sigma^3 f(\theta)}{3kT(\Delta G_v)^2} \right] \quad [11]$$

where I_0 is a pre-exponential factor (to be explained below), σ is the solid-liquid interfacial energy, and $f(\theta)$ is a wetting function that determines the extent of heterogeneity in the nucleation event, defined as, $f(\theta) = (2 - 3 \cos \theta + \cos^3 \theta)$. The nucleation probability, P_n in a volume v and in a time interval Δt is calculated using Poisson distribution [14],

$$P_n = 1 - \exp(-Iv\Delta t). \quad [12]$$

Li et al. [13] used the above nucleation model along with the Kim-Kim-Suzuki [15] PF model to simulate CET in Ni-Cu alloys. The PF method and the nucleation model used in this research is based on a similar approach.

The pre-exponential factor, I_0 , merits some explanation, because it has distinctly different values for homogeneous and heterogeneous nucleation in the melt. In the case of homogeneous nucleation, $f(\theta)$ is equal to 1.0, and I_0 is given by the product of the number of liquid atoms per unit volume, the atomic jump frequency, and number of atoms of liquid in contact with the surface of the embryo, captured in the same order in the following equation

$$I_0 = N_v \left(\frac{D_l}{a^2} \right) \left(\frac{4\pi R_{cr}^2}{a^2} \right) \quad [13]$$

where N_v is the number of atoms per unit volume is roughly N_{Av}/M_v , where N_{Av} is the Avogadro number and M_v . Since M_v for most alloys is of the 10^{-5} m^3 per mole and N_{Av} is 6.023×10^{23} atoms per mole, N_v is roughly of the order of 10^{28} atoms / m^3 . D_l , diffusivity in the liquid is of the order of $10^{-9} \text{ m}^2/\text{s}$ for most alloy melts. The atomic radius, a , is of the order of $3 \times 10^{-10} \text{ m}$. Therefore, the atomic jump frequency, $\left(\frac{D_l}{a^2} \right)$, is of the order of 10^{10} s^{-1} . The radius of the critical nucleus varies with thermodynamic undercooling. Assuming $R_{cr} = 10a$, the number of liquid atoms surrounding the embryo is of the order 10^2 . Therefore, based on the above analysis, I_0 for homogeneous nucleation is of the order of $10^{40} \text{ m}^{-3}\text{s}^{-1}$. Typically, I_0 is listed as $10^{39 \pm 1} \text{ m}^{-3}\text{s}^{-1}$ in the literature. In the case of heterogeneous nucleation, I_0 depends on N_s , the number of atoms per unit volume in contact with heterogeneous substrates in the liquid instead of N_v . Typically, $N_s \ll N_v$. In addition, the number of liquid atoms in contact with the surface of the embryo is also reduced because of the formation of a spherical dome. Values of $10^{30} \text{ m}^{-3}\text{s}^{-1}$ have been used in previous phase field simulations. In general, I_0 in this case has to be calibrated based on the experimentally observed grain size. It should be noted that in the case of heterogeneous nucleation, the $f(\theta)$ term has to be included in the evaluation of Equation. 10.

4.1.3 Implementation of the nucleation model

In order to implement the thermodynamically consistent nucleation model, the following procedure was used. For each lattice point in the liquid, the local liquidus and solidus temperatures were calculated based on the polynomial expressions shown in Figure 4. If the local temperature in the liquid is lower than the local liquidus temperature, the composition of the potential nucleus, C_s , is calculated based on Equation 10. The local thermodynamic driving force, ΔG_v , is calculated next based on the composition of the liquid and the solid nucleus composition. The critical nucleus size, R_{crit} is calculated using, $R_{crit} = 2\tilde{\gamma}/\Delta G_v$. All sites satisfying the condition $R \leq R_{crit}$ are identified, and the nucleation probability, P_n at the sites are calculated using Equations. 11 and 12. A random number generated between 0 and 1.0, P_r is compared against P_n , and the sites are designated as nuclei if $P_r < P_n$, and the site concentrations are set equal to C_s . The excess solute, $C_l - C_s$ is then distributed uniformly to all the existing liquid sites. This step is an approximation because it assumes just at one time step that the solute diffusivity in the liquid is

infinite. However, it serves as an efficient approach for linking the nucleation model with the existing PF framework. In the succeeding time steps, the sharp interface between the nucleus and the surrounding liquid evolves smoothly through the formation of the diffuse interface, and the consequent solute enrichment of the surrounding liquid is consistent with growth velocity of the nucleus. Homogeneous nucleation case is treated by assigning $f(\theta)$ equal to 1, and I_0 equal to $10^{39} \text{ m}^{-3}\text{s}^{-1}$ as described previously. The degree of heterogeneity in the nucleation is handled by simply changing the value of $f(\theta)$ as an adjustable parameter and letting I_0 equal to $10^{30} \text{ m}^{-3}\text{s}^{-1}$. There are more rigorous approaches to implementing heterogeneous nucleation in the liquid phase [16] by explicitly treating nucleation on an external wall of a particle, but such approaches are time-consuming and cannot be implemented at the length scales the current simulations are performed.

4.2 DEMONSTRATION OF THE PF CET SIMULATIONS FOR TI-CU ALLOY

The objective of the initial set of PF simulations was to establish that the nucleation model and the thermodynamic integration of MEUMAPPS-SL with Ti-Cu binary alloys would demonstrate the expected CET behavior in the alloy. Specifically, the focus was on making sure that the random orientations of the equiaxed dendrites were captured accurately, and the excess solute rejected by the nuclei were handled properly in the numerical implementation. For these initial simulations, the following nucleation parameters, characteristic of heterogeneous nucleation with a highly wetting “substrate” in the liquid was assumed in order to obtain an accelerated nucleation condition for easy verification and validation. The parameters used in the MEUMAPPS-SL simulations are shown in Table 1. In this simulation, the substrate was a thin layer of solid of the average alloy composition Ti-0.06Cu (all compositions used in the simulations are given in atom fraction). The initial temperature at the solid-liquid (s-l) interface was chosen as 1830K, which is 14K lower than the liquidus temperature of the alloy. One of the objectives in the initial simulations was to develop some insight on how to adjust the nucleation parameters to obtain the occurrence of CET, and to match the grain size observed in the DED experiments. Table 1 shows the parameters used in the initial CET investigations.

Table 1. PF parameters used in the initial CET investigations

Parameter	PF input
Mesh Resolution	10^{-8} m
Time Step	$5 \times 10^{-9} \text{ s}$
Domain Size	$1000 \times 5000 \text{ mesh}$
Alloy Composition	Ti-0.06Cu
Alloy Solidus	Calculated from polynomial in Fig. 4
Alloy Liquidus	Calculated from polynomial in Fig. 4
Diffusion Coefficient	$2 \times 10^{-9} \text{ m}^2/\text{s}$
Nucleation Parameters	$I_0 = 10^{31} \text{ m}^3/\text{s}$; $f(\theta) = 0.002, 0.005$
Thermal Conditions	$G = 386662 \text{ K/m}$; $R = 0.05 \text{ m/s}$

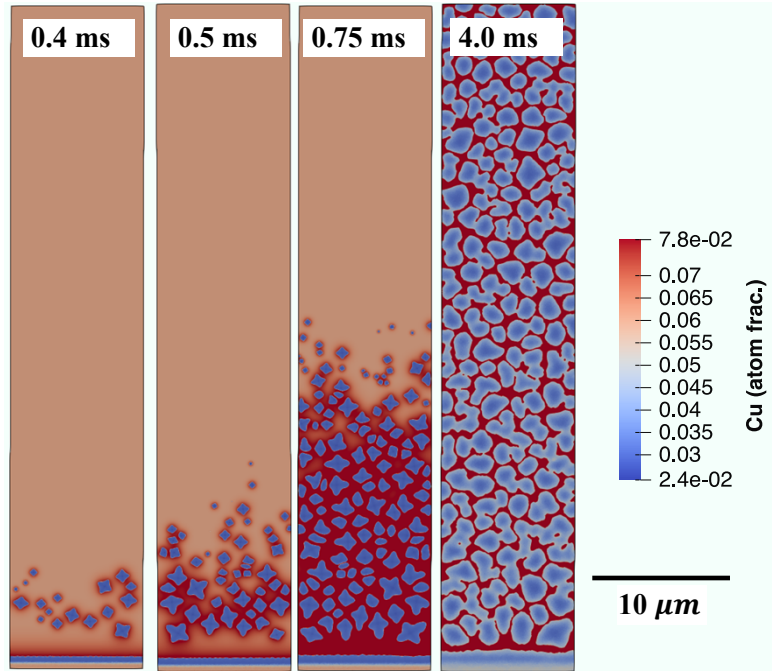


Figure 5. Bulk nucleation and evolution of CET during solidification of a Ti-0.06Cu alloy using PF parameters shown in Table 1. Copper concentration contours are shown after various solidification times.

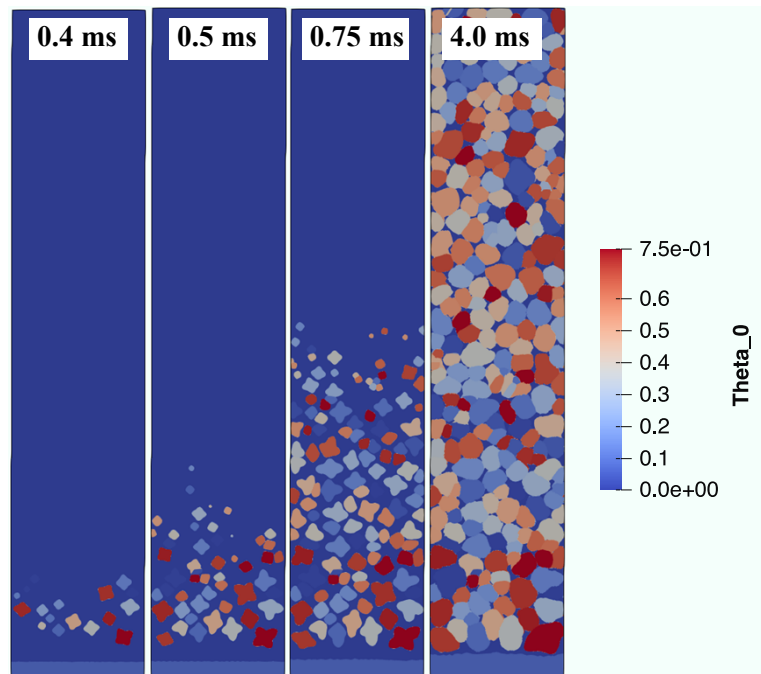


Figure 6. Grain orientation angles of the evolving nuclei shown in Figure 5 above.

Figure 5 shows the nucleation of equiaxed grains in the bulk liquid ahead of the epitaxial solidification front emanating from the bottom of the domain using the PF simulation parameters shown in Table 1. The simulations are able to capture the rejection of the solute copper from the nuclei, and the enrichment of

the surrounding liquid with solute. The solute enrichment seems to trigger local undercooling, which in turn promotes additional nucleation in its vicinity, leading to the formation of a fully equiaxed grain structure. Another feature of the MEUMAPPS-SL simulations is the formation of equiaxed grains with random crystallographic orientations. The nuclei orientations are assigned to the liquid sites surrounding the nuclei in a dynamic fashion so that they grow with the initially assigned orientation for each nucleus. The resulting grain orientation evolution based on the composition evolution is shown in Figure 6. Figure 6 shows just the rotation angle of the grain, while the full orientation of each grain is defined in the code based on the rotation angle and the direction cosines of the rotation axis.

Since the width of the simulation domain in Figures 5 and 6 is $10\text{ }\mu\text{m}$, the average grain size obtained in the simulations is roughly $1.5\text{ }\mu\text{m}$. A third test of the nucleation model is to verify that changing the nucleation parameters would allow us to tune the equiaxed grain size so that it can match the grain size obtained in the DED experiments of Zhang et al. [3], in which they obtained an equiaxed grain size of roughly $10\text{ }\mu\text{m}$ under the thermal conditions used in their DED process. In order to check the sensitivity of the nucleation parameters on the CET grain size, the above simulations were repeated with $f(\theta) = 0.005$, keeping all other parameters constant. The simulation width in this case was reduced to $5\text{ }\mu\text{m}$. The higher value for $f(\theta)$ implies that the nucleation in this case is a bit more difficult than for the previous case. This allows the epitaxial solidification front to progress a bit more in the previous case before the undercooling sufficient for nucleation is obtained. This results in a slightly larger mean grain size of roughly $2\text{ }\mu\text{m}$. The results are shown in Figure 7.

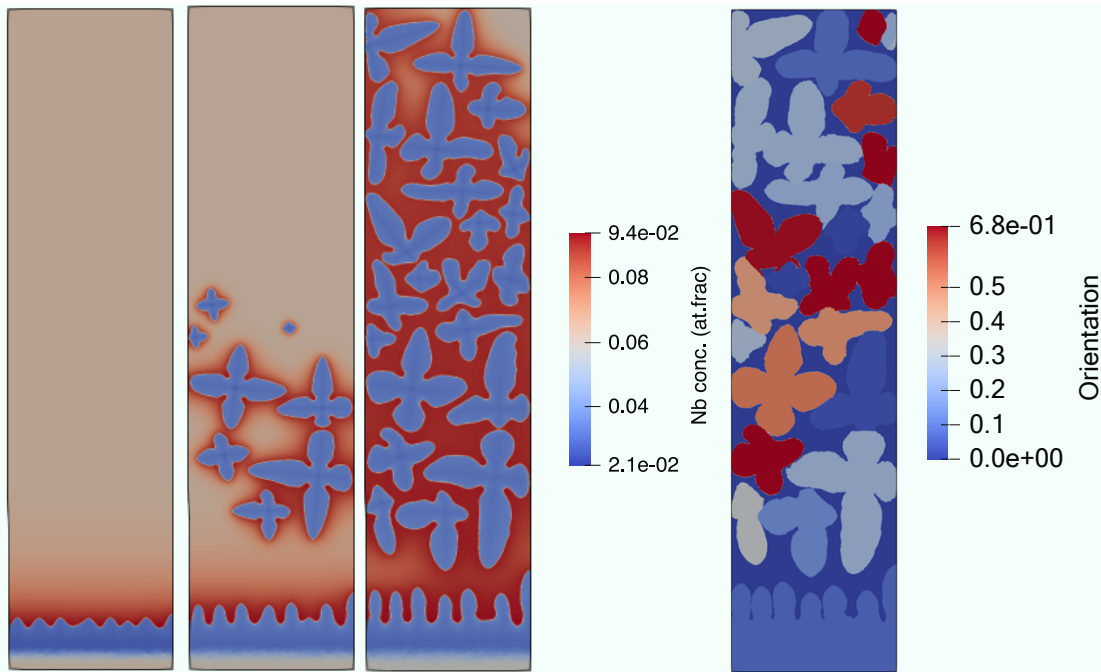


Figure 7. Increase in CET grain size due to decreasing nucleation density introduced by changing the nucleation parameter. The grain size is larger than in Figures 5 and 6.

One of the features of the CET seen in the simulations is that the equiaxed grains that nucleate at the earliest time, i.e., closest to the columnar front, do not physically impinge against the columnar grains. It appears that the growth rate of the equiaxed grains decrease with increasing solute enrichment ahead of the dendrite tips and stop before a physical impingement occurs. This observation is somewhat different from the original theory of Hunt [17] in which a physical impingement is assumed. The results shown in Figures 6 and 7 are for an arbitrary choice of G and R that was not typically obtained during the

solidification of the melt pool. The $G(t)$ and $R(t)$ combinations obtained by thermal modeling of the melt pool solidification (Figure 3) are shown below in Table 2.

Table 2. Time dependent G and R as a function of solidification time of melt pool

Solidification Time (s)	Temperature Gradient (K/m)	Solidification rate (m/s)
0.000000000	502739.969	0.005513039
0.027400017	502739.969	0.005513039
0.040500015	435342.25	0.007263276
0.046099991	394000.25	0.026033382
0.047300011	348131.938	0.029033573
0.048200011	324571.063	0.029520024
0.048900008	308534.625	0.024778723
0.049500018	413457.969	0.016104577
0.050099999	384111.25	0.015000805
0.050300002	386662.781	0.014197815

For extracting the $G(t)$ and $R(t)$ values from the thermal simulations, the isotherm corresponding to 1820K was used which is close to the liquidus temperature of the Ti-0.06Cu alloy.

4.3 APPLICATION OF VALIDATED PHASE FIELD MODEL TO TI-CU AM GEOMETRIES

During AM of a component with a complex geometry the local cooling rate will depend on the local cross-section of the solid sections in the active layer resulting in a range of G and R conditions. Performing a melt-pool scale thermal model to calculate the effect of local cross section on melt-pool solidification rate was beyond the scope of this project. However, in order to capture the effect of varying solidification rates and temperature gradients, the range of G and R values during solidification of a single melt pool was used to drive the PF simulations to calculate the effect varying thermal conditions on CET. The $G(t)$ and $R(t)$ values obtained during different solidification times at the center line of the melt pool shown in Figure 3 are captured in Table 2. PF simulations were performed using each of these G and R sets as constants during PF simulations, in order to develop a deeper insight into their effect on the transient solidification of the epitaxial front, the nucleation of solid grains in the bulk liquid, and their evolving morphologies. In addition, simulations were also performed by keeping a constant set of G and R , and varying the nucleation parameters, I_0 and $f(\theta)$ to capture their effect on CET.

4.3.1 Effect of G and R on CET

In order to understand the effect of G and R on CET, different sets of G and R from Table 2, were used to drive separate PF simulations. These simulations were performed using ORNL Summit using 128 nodes with a wall clock time of 12 hours per simulation. The nucleation parameters were $I_0 = 10^{31} \text{ m}^3/\text{s}$ and $f(\theta) = 0.005$. The PF simulation results are shown in Figure 8 for $G = 348132 \text{ K/m}$ and $R = 0.029 \text{ m/s}$.

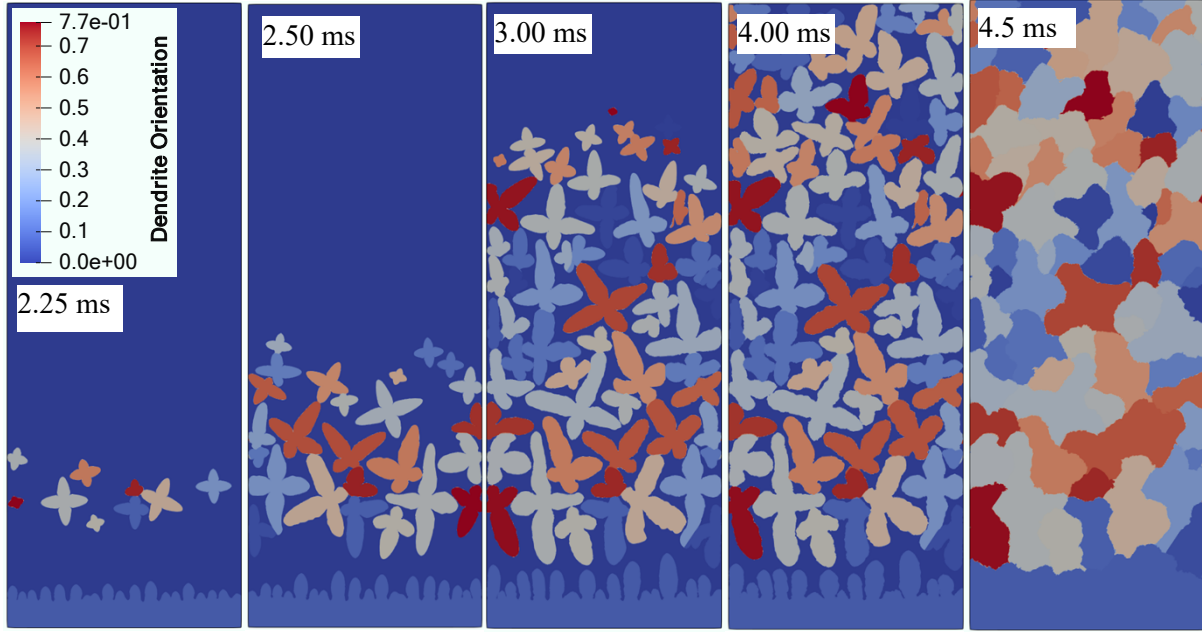


Figure 8. Temporal evolution of CET in Ti-0.06Cu alloy using $G = 348132$ K/m and $R = 0.029$ m/s showing fully equiaxed microstructure.

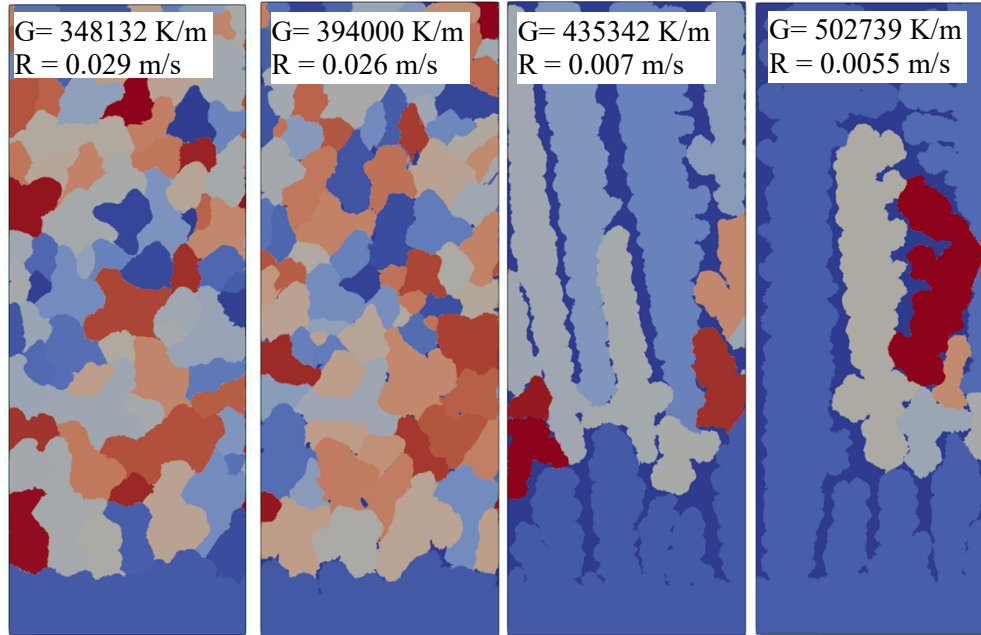


Figure 9. Transition in the solidification microstructure from fully equiaxed to columnar grains with different orientations than in the substrate due to bulk nucleation in the liquid.

It can be seen from Figure 8, that for the assumed nucleation parameters, CET occurs during solidification and the columnar zone is completely blocked by the growth of equiaxed grains. The mean diameter of the equiaxed grains is about $3.0 \mu\text{m}$. CET occurs initially at a characteristic distance from the tip of the columnar front that generates the extent of undercooling required for nucleation.

Typical solidification morphologies obtained for different combinations of G and R in Table 2 are shown in Figure 9. Figure 9 shows that the solidification microstructure due to bulk nucleation in the liquid transitions from fully equiaxed grains from left to elongated grains in the right, with increasing G and decreasing R . The orientations of the columnar grains in the extreme right microstructure are different from that of the base orientation, that gives rise to a different solidification texture. This transition behavior is similar to ones observed previously in simulations [18]. In practice, this transition helps to understand the development of solidification texture in columnar dendrites where the crystal orientations are completely different from the orientations in the substrate. In the absence of bulk nucleation in the liquid, the orientations in the columnar structure would only be a subset of the initial orientations in the substrate subject to grain elimination due to competitive growth.

From Figure 9, it can be seen that the nucleation of the grains in the bulk liquid occurs after increasing extents of growth of the epitaxial columnar front as the G/R ratio is increased. The reason for the enhanced nucleation under lower G/R ratio as discerned from an analysis of the PF simulations of the Cu concentration field and the temperature field are provided in sections 4.3.2 and 4.3.3.

4.3.2 Effect of Cu content on CET in Ti-Cu Alloys

The simulations shown in Figures 8 and 9 were extended to larger simulation domains containing multiple grain orientations in order to understand the effect of base grain orientation on CET. Also, since the nucleation model is linked to the alloy thermodynamics it allows determination of the alloy chemistry on CET, for a given set of composition independent nucleation parameters, I_0 and $f(\theta)$. Figure 10 shows the Ti-rich end of the Ti-Cu phase diagram as determined by the SSOL4 database used in ThermoCalc. The Calphad functions for the liquid and BCC-B2 phase used in PF simulations were also obtained from the SSOL4 database, to be consistent. Three different Ti-Cu alloys with 0.03, 0.06, and 0.08 mass fraction of Cu as indicated in the phase diagram. There is an increase in the equilibrium solidification range on creasing the Cu content. In addition, the liquidus slope increases continuously with Cu content.

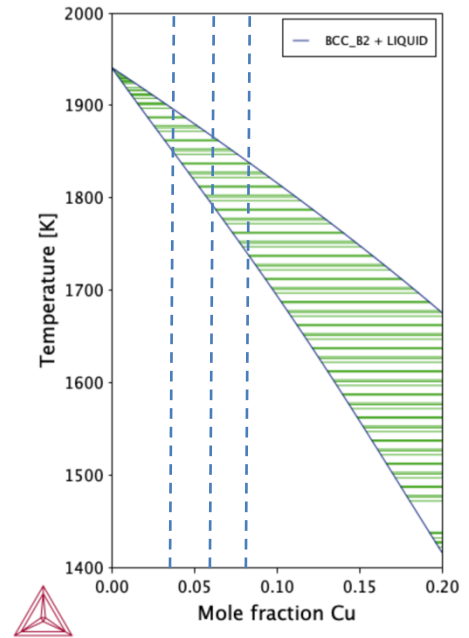


Figure 10. Titanium-rich end of the Ti-Cu phase diagram calculated using SSOL4 database in ThermoCalc. The three Ti-Cu alloys used in the PF simulations.

PF simulations of solidification were performed for the three alloys using large simulation domains, that allowed multiple grains to be realistically accommodated in the substrate. The simulation domain consisted of $10,000 \times 3,000$ points with a mesh spacing of 10^{-8} m, corresponding to a physical dimension of $100 \mu\text{m} \times 30 \mu\text{m}$. Five seed grains were introduced at the bottom substrate layer corresponding to a grain diameter of $20 \mu\text{m}$. The nucleation parameters were $I_0 = 10^{39} \text{ m}^3/\text{s}$ and $f(\theta) = 0.01$. Constant thermal conditions of $G = 394000 \text{ K/m}$ and $R = 0.0290 \text{ m/s}$ were used to drive the PF simulations. Figure 11 shows the simulated grain structure for the Ti-0.03 Cu alloy.

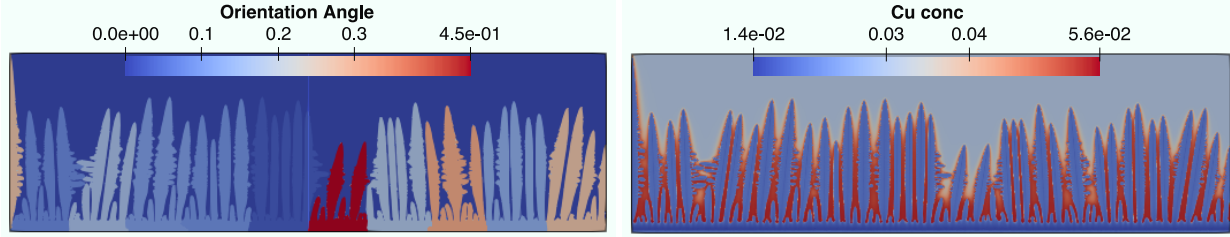


Figure 11. Simulated solidification microstructure for Ti-0.03Cu showing the dendrite orientations (left) and the Cu concentration field (right).

As seen from Figure 11, CET was not initiated for Ti-0.03Cu alloy during solidification under the thermal conditions and nucleation parameters used in the simulations. The ability of the PF code to simulate dendrite evolution from multiple base grain orientations can be seen clearly. Solute Cu enrichment is seen between the columnar dendrites and ahead of the dendrite tips. The maximum Cu concentration in the enriched regions is 0.0056 as seen from the legend bar. This is consistent with the phase diagram shown in Figure 10. It is clear that under the solidifications, the constitutional undercooling obtained in the liquid ahead of the columnar front was not sufficient to nucleate grains in the bulk liquid. When the Cu concentration is increased to 0.06, the solidification range as well as the maximum concentration in the liquid at the solidus temperature increase. Since the level of saturation of the liquid with Cu increases in this case compared to the 0.03Cu alloy, the probability for nucleation in the liquid increases. The same argument is true for the 0.08Cu alloy that has a further increase in the solidification range and the level of Cu rejected into the liquid ahead of the dendrite tip at the solidus temperature. Figures 12 and 13 show the solidification microstructures of the Ti-0.06Cu and Ti-0.08Cu alloys clearly indicating the equiaxed dendrites forming from bulk nucleation.

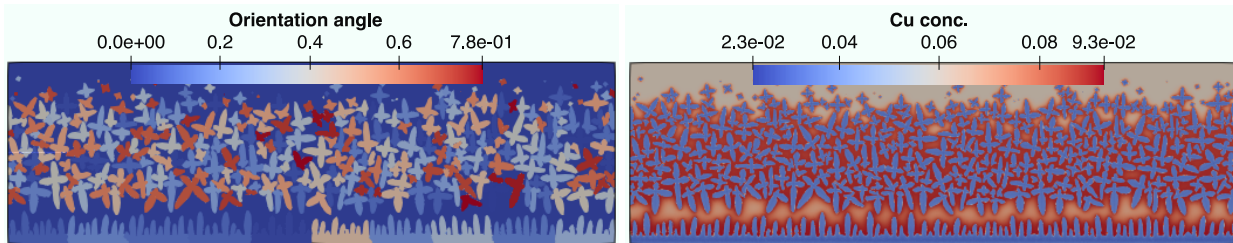


Figure 12. Simulated CET microstructure during solidification of Ti-0.06Cu alloy showing dendrite orientations (left) and Cu concentration field (right).

Figure 12 shows that for the Ti-0.06Cu alloy equiaxed grains begin to nucleate in the liquid after the columnar growth from the substrate grains is initiated and some amount of columnar growth has occurred. The scale of breakdown in the initial planar surface is such that a few columnar dendrites are initiated in each grain. Grain nucleation in the liquid occurs prior to any significant grain competition occurring between the columnar grains. For the grain orientations used in the simulation, the presence of multiple grain orientations did not have a significant effect on the extent of CET. The nucleation density in the liquid is higher than what is required to produce a mean grain size of $20\mu\text{m}$, observed in the experiments. In the current simulations, the mean equiaxed grain size is roughly $2\mu\text{m}$. Similar results are obtained for the Ti-0.08Cu alloy as shown in Figure 13.

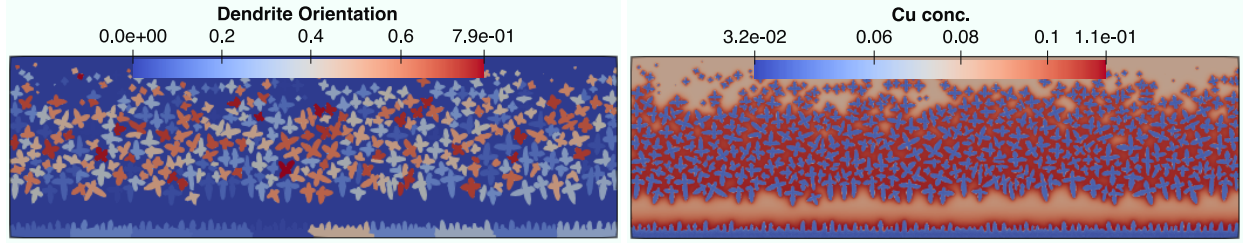


Figure 13. Simulated CET microstructure during solidification of Ti-0.08Cu alloy showing dendrite orientations (left) and Cu concentration field (right).

There is no significant difference in the grain size of the equiaxed grains for the 0.06 and 0.08Cu alloys as seen by comparing Figures 12 and 13, although the onset of CET appears to have occurred after lower extent of columnar growth in the 0.08Cu alloy compared to the 0.06 Cu alloy. The differences between the three alloys in terms of solidification kinetics and the onset of CET can be better understood through a temporal and spatial analysis of the microstructural and temperature fields obtained through the PF simulations, shown in Figure 14.

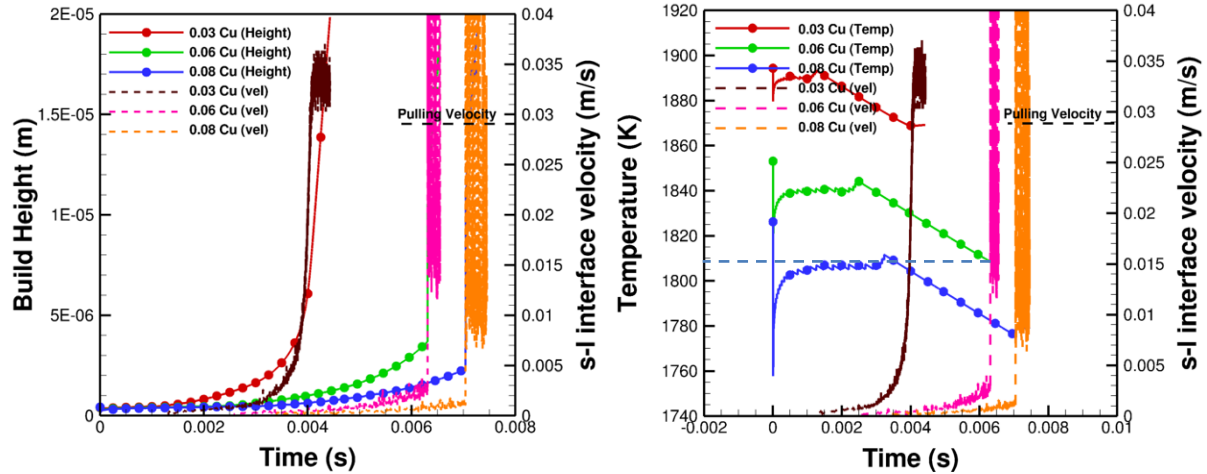


Figure 14. Temporal evolution of solidification height and s-l interface velocity, V (left) and s-l interface temperature (right). The constant imposed solidification rate (pulling velocity) is marked in the figures.

Figure 14 (left) shows the variation of solidification height as a function of simulation time. For the Ti-0.03Cu alloy that shows no CET, the solidification height (solid red curve) increases slowly initially, but then accelerates significantly due to the destabilization of the planar interface. During this period, the solid-liquid (s-l) interface velocity, V , as measured by the velocity of the tallest dendrite / cell tip in the microstructure (black, dotted curve) goes above the imposed solidification rate, R (termed as the pulling velocity, indicated in the plots as a horizontal line at 0.029 m/s) that is imposed on the system to drive the PF simulations. Therefore, it is clear that the microscopic response of the system is very different from the imposed R . R was calculated based on a melt-pool scale thermal simulation, with a simple linear model for latent heat that assumes that the latent heat released is proportional to the dimensionless

undercooling, $(T - T_S) / (T_L - T_S)$, where T_S is the solidus temperature, T_L is the liquidus temperature and T is the local temperature. However, V is determined by the local thermodynamic driving force and the mobility of the s-l interface that are microscopic quantities. The initial drastic temperature drop at the s-l interface shown in Figure 14 (right) is due to the melting of the substrate since the initial temperature

of the liquid is at T_L . The s-l interface temperature drops to a temperature below the liquidus, at which point before solidification in the build direction starts. The interface temperature rises because of the rapid re-solidification that occurs, during which the partitioning of Nb to the liquid is not significant. The s-l interface temperature then drops continuously associated with the increase in V . The solidification process in this regime is transient since V increases very rapidly due to the destabilization of the initially planar interface and the formation of the cell / dendrite structure. Steady state seems to occur after the overshoot in V is eliminated, and V approaches R . In Figure 14 (right) initiation of nucleation is indicated as a sharp discontinuity in V as the tip of the tallest dendrite shifts suddenly from the columnar base grains to the equiaxed grain that forms much higher in the liquid column. However, for the assumed nucleation parameters there is no occurrence of nucleation in the bulk liquid for Ti-03Cu alloy, consistent with the grain structure in Figure 11. In the case of 0.06Cu and 0.08Cu alloys, the dendrite tip temperature undergoes a similar evolution as for the 0.03Cu alloy. However, liquid nucleation in the liquid occurs with a jump in V as soon as the interface begins to destabilize and the columnar dendrites begin to form, consistent with Figures 12 and 13. The undercooling in the liquid ahead of the fastest growing dendrite tip for the three alloys is shown Figure 15.

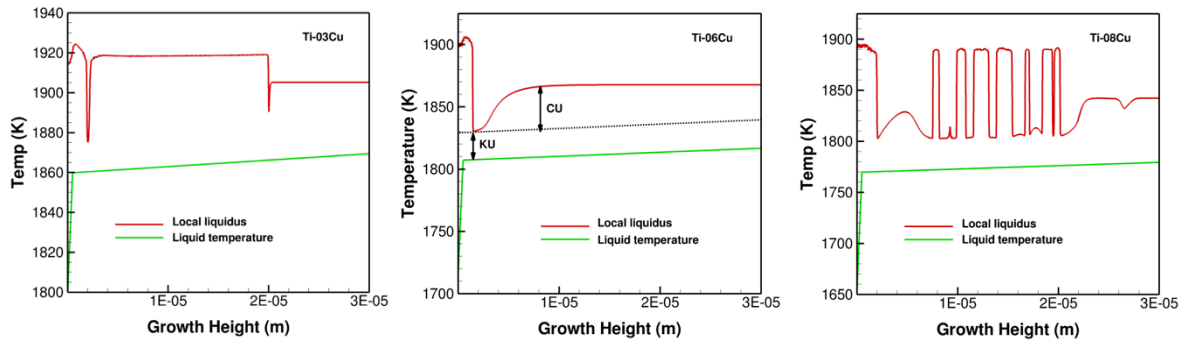


Figure 15. Spatial temperature distribution during solidification of Ti-0.03Cu (left), Ti-0.06Cu (middle) and Ti-0.08Cu (right) showing the undercooling in the liquid ahead of the epitaxial front.

In Figure 15, the red curve is the local liquidus temperature based on the local Cu concentration in the liquid. The actual temperature in the liquid as a function of height is given by the green curve. The total local undercooling in the liquid is the difference between the red and green curves. For the Ti-03Cu alloy, the shape of the liquidus curve can be explained by examining the structure along the vertical line that was used to calculate the local liquidus temperatures. As shown in Figure 16 (left), the initial high liquidus temperature corresponds to the liquidus temperature of the Cu-lean dendrite that forms at the bottom of the simulation domain. The sudden initial drop in the liquidus temperature is due to the intersection of the line with a solute rich interdendritic liquid at the bottom of the dendrite. The liquidus temperature increases again because the vertical line stays inside the solid dendrite. The second drop in the liquidus temperature occurs close to the tip of the dendrite as it meets the bulk liquid. It is clear that there is hardly any evidence of constitutional undercooling in front of the dendrite tip in the Ti-03Cu alloy. However, there is thermal undercooling, since V cannot keep pace with R , as described previously. The total undercooling in the alloy ranges roughly from 50K to 60K in the liquid mainly due to the thermal undercooling. However, based on the nucleation parameters, the undercooling is not sufficient to initiate bulk nucleation.

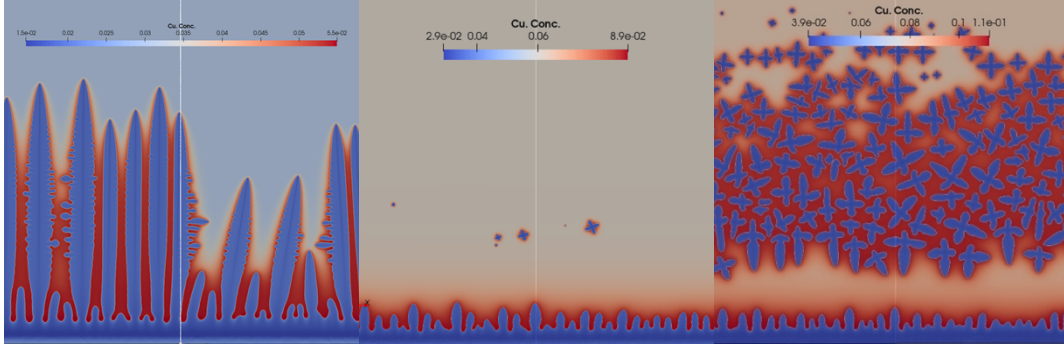


Figure 16. Magnified sections of Figures 11-13, showing the dendritic structure along the vertical line used for calculating the local liquidus temperatures. Left – 0.03Cu, Middle – 0.06Cu and Right – 0.08Cu.

For the Ti-0.06Cu alloy, the total undercooling indicated in Figure 12 corresponds to a time at which bulk nucleation in liquid just starts to occur, as shown in the middle of Figure 16. The total undercooling in the liquid at a location close to the nucleus is roughly 57K. It is evident that for the Ti-0.06Cu alloy nucleation in liquid occurs at a lower undercooling than in Ti-0.03Cu. For the Ti-0.08Cu alloy, the total undercooling for nucleation is roughly the same as that for Ti-0.06Cu. It is also significant to note that the thermal undercooling (TU) plays a significant role in addition to constitutional undercooling (CU) marked for the Ti-0.06Cu alloy. CU and TU for the alloy were measured to be 35K and 22K, respectively.

4.3.3 Effect of Time Varying G and R on CET

The above simulations were extended to time dependent $G(t)$ and $R(t)$ using Ti-0.06Cu alloy shown in Table 2. The simulations were performed in the Eagle supercomputer at NREL. The simulation domain consisted of 10000×15000 mesh points with a mesh spacing of 10 nm, representing a physical dimension of $100 \mu\text{m} \times 150 \mu\text{m}$. The simulations required a clock time of roughly 48 hours using 18,432 Eagle cores (512 nodes). The objective of the simulations was to determine the effect of time varying thermal conditions during solidification on the onset of bulk nucleation. In the runs shown above where the objective was to investigate the effect of alloy chemistry, the largest R and smallest G in Table 2 was used. However, during the actual solidification of the melt pool, R increases from a low value and G decreases from the highest value as shown in Table 2. This is expected to have an effect on the rate of movement of the isotherms relative to the rate of movement of the s-l interface (V) and therefore on the thermal undercooling (TU) before the onset of liquid nucleation. The microstructures obtained just prior bulk nucleation and after complete coverage of the domain with equiaxed grains is shown in Figure 17. The initial nuclei in the liquid form after the initiation of the columnar growth in the base grains as before.

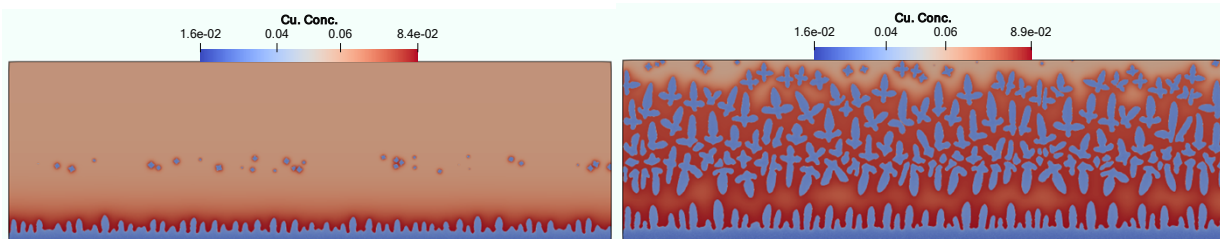


Figure 17. Cu concentration profile at the start of the nucleation (left) and structure after longer solidification time in Ti-0.06Cu solidified with variable G and R from Table 2.

Figure 17 shows that the onset of nucleation occurs at approximately the same distance from the columnar front, indicating that a constant nucleation undercooling is required to trigger nucleation for the assumed set of nucleation parameters. An analysis of the total undercooling at this location based on the difference between the actual temperature and the local liquidus temperature indicates values ranging from 44K - 45K. In this case, the dendrite tip temperature at the onset of nucleation, T_U is seen to be roughly 1,818K as indicated by the dotted line in Figure 18. This is roughly 10K higher than the dendrite tip temperature shown in Figure 15. The change in the T_U and C_U is a combined effect of the variable G and R as well as the reduction in $f(\theta)$ from 0.01 used earlier to 0.005. The effective grain size, however, has not changed compared to Figure 12.

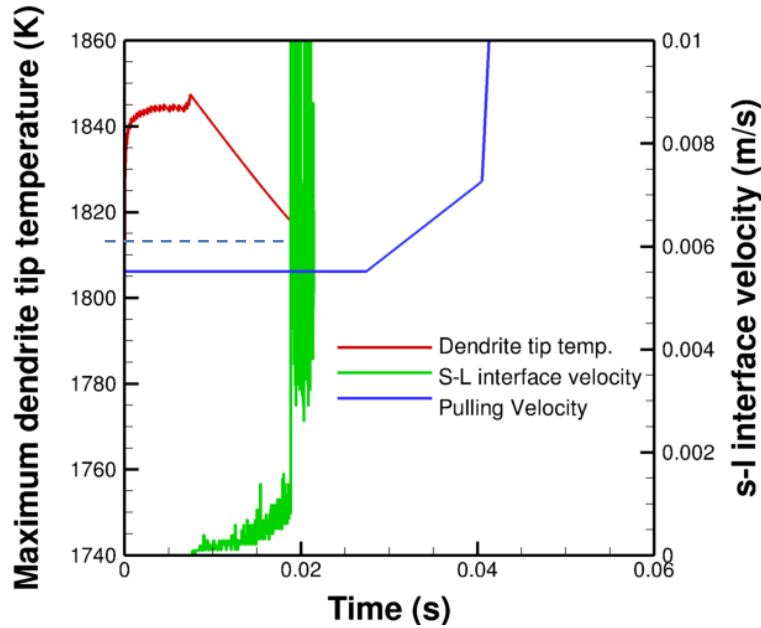


Figure 18. Interface velocity (V) (right) and dendrite tip temperature (left) as a function of solidification time for the solidification condition shown in Figure 17.

In previous simulations (Figure 9) the effect of using different combinations of G and R on the CET morphology was presented keeping the nucleation parameters constant. As a subsequent study, the effect of changes in nucleation parameters, I_0 and $f(\theta)$, keeping G and R constant was undertaken. The simulations were performed for Ti-0.06Cu alloy in a domain of 3000×3000 mesh points with a mesh resolution of 10 nm. The thermal conditions were $G = 394000$ K/m and $R = 0.026$ m/s. Figure 19 summarizes the effect of nucleation parameters on the nucleation undercooling and the resulting grain morphology. As $f(\theta)$ increases, the degree of heterogeneity decreases that leads a high nucleation undercooling required to stimulate CET. It was found that for $f(\theta) > 0.02$, CET failed to occur. It appears that as the nucleation undercooling increases, the grains that nucleate in the liquid also begin to elongate. For $f(\theta) = 0.015$, the nucleated grains are elongated significantly, and almost become indistinguishable from the epitaxially growing columnar grains. However, as shown in Figure 9, the crystallographic orientation of the nucleated grains are random, and therefore they can be separated from the epitaxially growing dendrites that have the same orientation as the base grain from which they form.

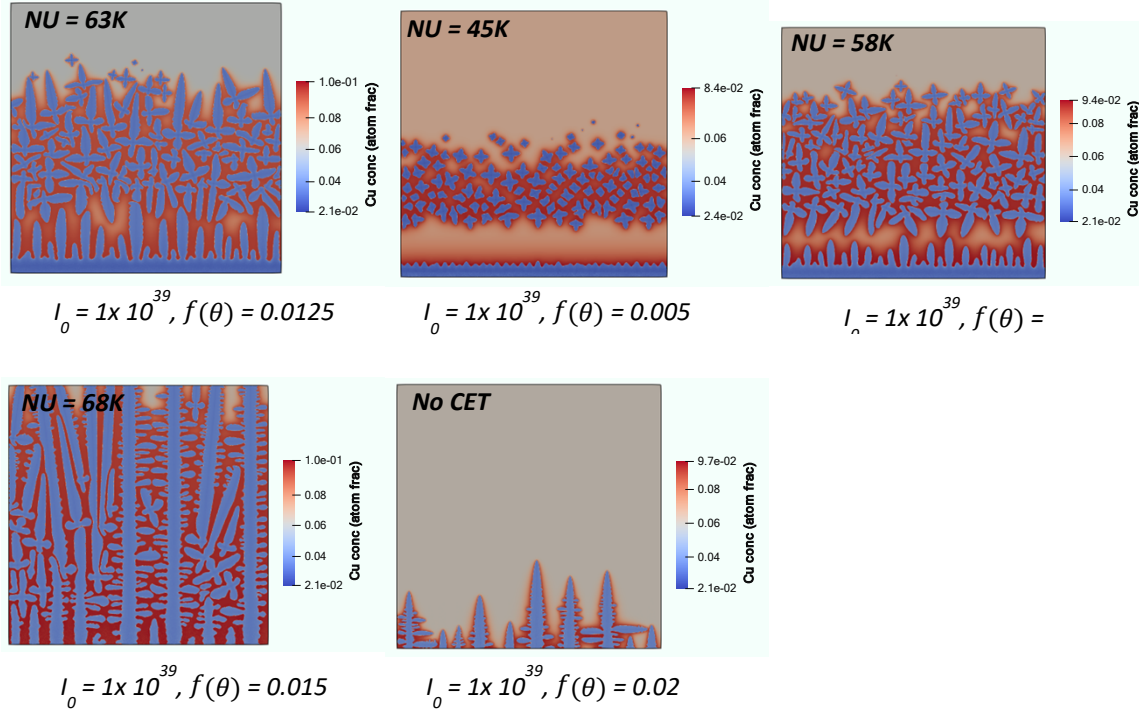


Figure 19. Effect of heterogeneous nucleation parameters on the morphology of CET grains.

4.4 CET SIMULATIONS IN TI-NB-CU TERNARY ALLOYS

In order to perform simulations in a ternary Ti-Nb-Cu alloy, the Calphad based free energy functions were obtained from SSOL4 database in ThermoCalc in a form similar to the ones shown in Equations 2-8 above for the binary Ti-Cu alloy. The nucleation model was modified to account for the partitioning of both Cu and Nb in the liquid, and the redistribution of the elements from the solid nucleus into the liquid phase as done previously for the binary alloy. The modified code was used to perform a parametric study of the effect of varying G and R and Nb concentration on nucleation in the liquid, and the resulting morphologies of the nucleated grains.

These simulations were run in a relatively small domain of 200×1500 mesh points with a mesh spacing of 10 nm. There are two distinct differences between the earlier simulations and the present one in terms of how the temperature gradient is applied. For the present simulations, the temperature gradients in the liquid and solid portions were assumed to be the same. However, in the earlier simulations, the temperature gradient in the solid was steeper, since it was assumed that the bottom edge of the substrate was equal to the solidus temperature at $t=0$, and the temperature at the s-l interface at $t=0$ was assumed to be equal to the liquidus that led to significantly reduced melting of the solid before solidification started to occur in the positive direction. However, in the current simulations, it was assumed that the temperature gradients in the solid and the liquid at the s-l interface were the same. Since the initial temperature of the s-l interface is the liquidus temperature, and temperature gradient in the solid is now significantly smaller, a significant amount of remelting of the substrate occurs before solidification starts to occur in the build direction. In order to prevent the complete melting of the solid substrate, the computational domain was translated down with the same velocity at which the s-l interface melted. When the solidification occurred, the computational domain was translated up with the solidification

velocity. The up and down translation of the domain helped in keeping the s-l interface roughly at the same height when melting or solidification occurred. The upward translation of the domain was stopped once the liquid nucleation occurred, and subsequent solidification occurred in a stationary domain. The

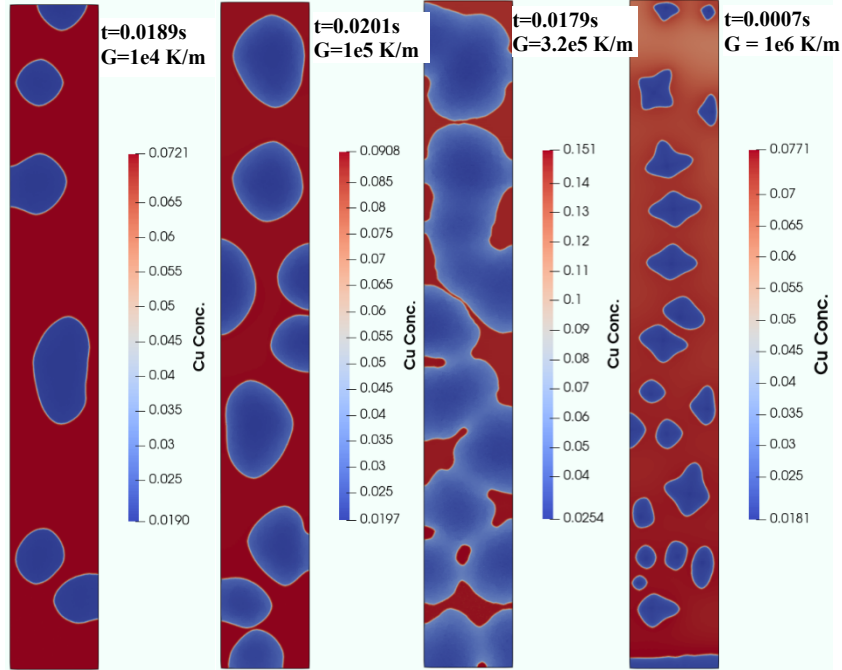


Figure 20. Bulk nucleation in the liquid for Ti-0.2Nb-0.06Cu alloy for $V = 0.029$ m/s for various G values.

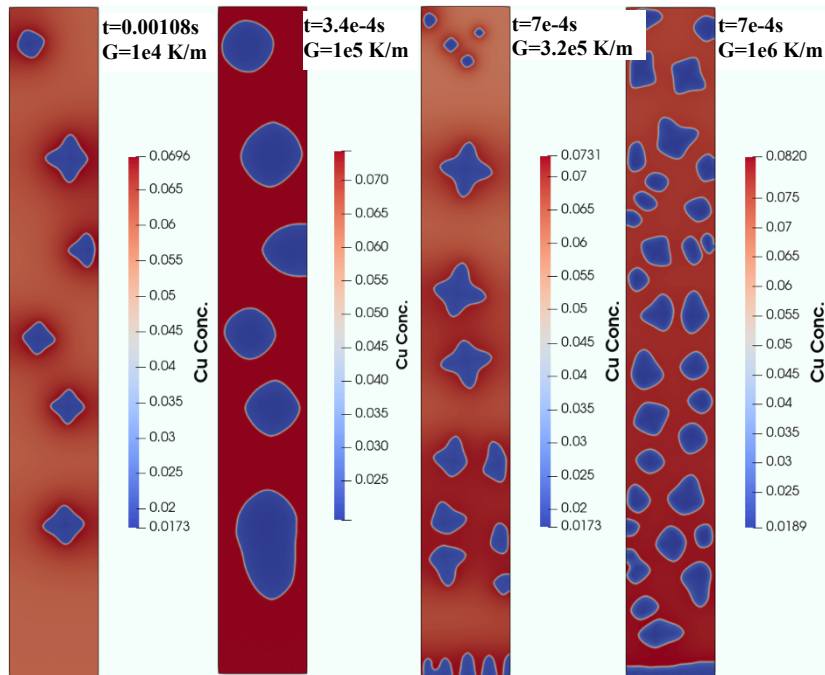


Figure 21. Bulk nucleation in the liquid for Ti-0.2Nb-0.06Cu alloy for $V = 0.05$ m/s at various G values.

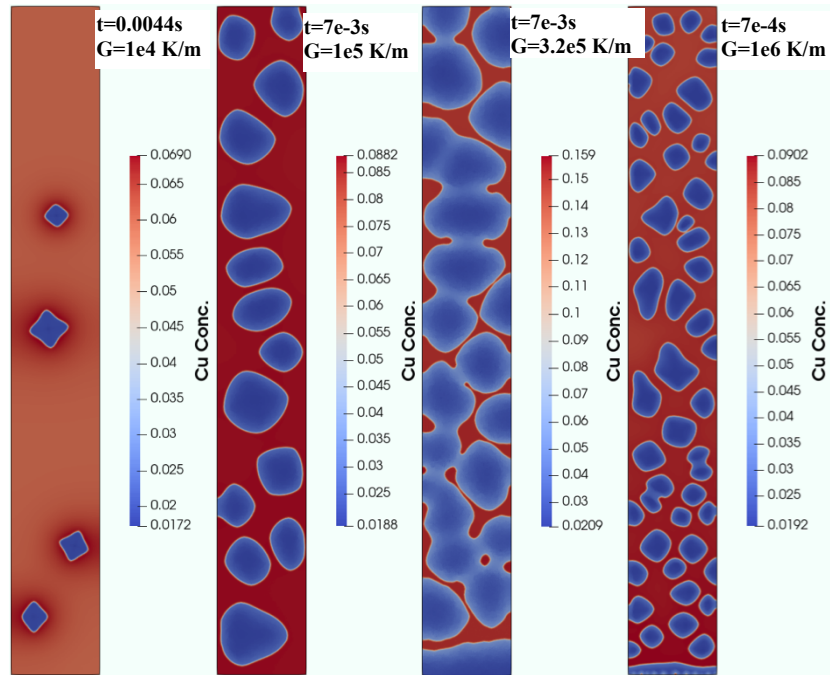


Figure 22. Bulk nucleation in the liquid for Ti-0.2Nb-0.06Cu alloy for $V = 0.08$ m/s at various G values.

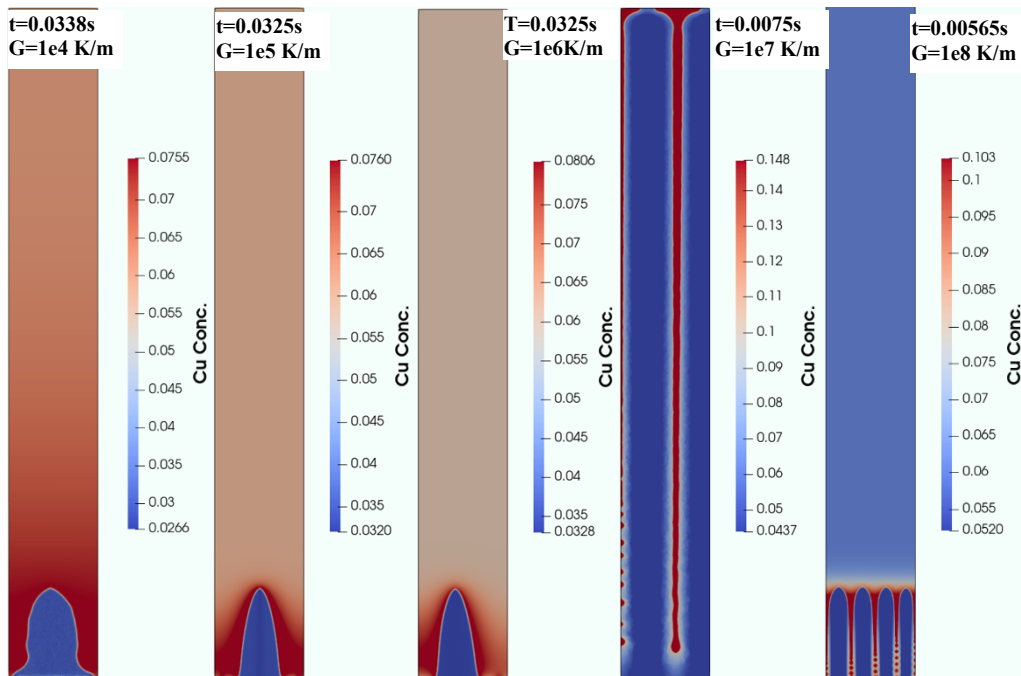


Figure 23. Bulk nucleation in the liquid for Ti-1e-5Nb-0.06Cu alloy for $V = 0.01$ m/s at various G values.

translation of the domain resulted in a significant saving in computational load, especially at low temperature gradients where significant remelting of the substrate occurs before solidification begins.

The simulations were performed for alloys with two levels of Nb, 10^{-5} (low-Nb) and 0.2 (high-Nb). For the low-Nb alloy, three imposed R values, 0.029 m/s, 0.05 m/s, and 0.08 m/s were used, and for each R three different G , 10^4 , 10^5 , 3.2×10^5 , and 10^6 K/m were used. For the high-Nb alloy, $R = 0.01$ m/s, 0.05 m/s and 0.08 m/s, and $G = 10^4$, 10^5 , 10^6 , 10^7 and 10^8 K/m were used. The simulation results for the high-Nb alloy are shown in Figures 20-22. The results show that nucleation in the liquid and the formation of equiaxed grains occurred for the high-Nb alloy for all the G and R input conditions used. The simulations also indicate that the nucleation density in the liquid increases with G at a given R , probably due to the increasing cooling rate. The nucleation density increased systematically from the lowest value of $G \times R$ to the highest, indicating that the total undercooling in the liquid required for nucleation was reached under all these conditions.

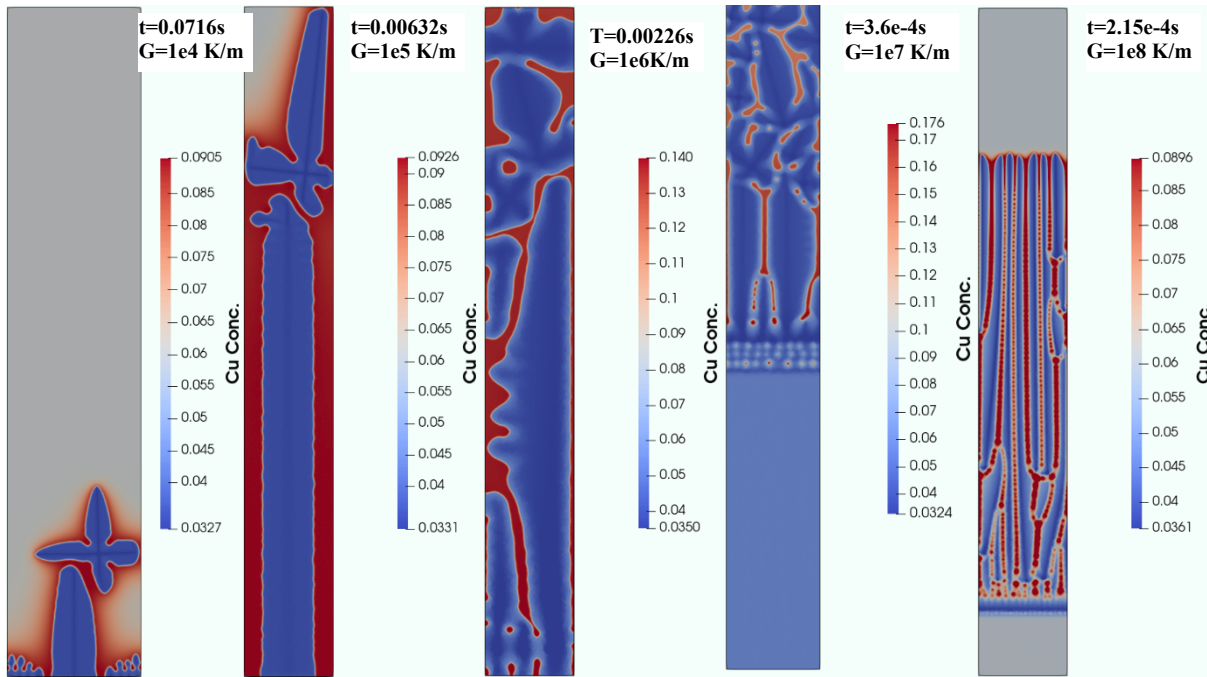


Figure 24. Bulk nucleation in the liquid for Ti-1e-5Nb-0.06Cu alloy for $V = 0.05$ m/s at various G values.

The evolution of solidification microstructures for the low-Nb alloy are shown in Figures 23-25. For $V = 0.01$ m/s, (this condition was not included for the 0.2Nb-0.06Cu alloy), there is no indication of bulk nucleation in the liquid. The steady state microstructure remains essentially columnar (cellular) with decreasing cell spacing with increasing cooling rate. The simulations appear to indicate the occurrence of some bulk nucleation for $G = 1e7$ K/m because the translation of the domain was stopped, and the cellular grains continued to grow to the top edge of the domain. Since the stopping of domain translation is triggered only when bulk nucleation occurs, it is evident that a stary nucleation event occurred, but it was fully dominated by continued cellular growth. For $V = 0.05$ m/s and $V = 0.08$ m/s, there is evidence for bulk nucleation for all cases investigated, with the nucleation rate increasing as a function of cooling rate. There is a transition in the morphology of the bulk nucleated grains from equiaxed to columnar for $G > 1.e7$ K/m.

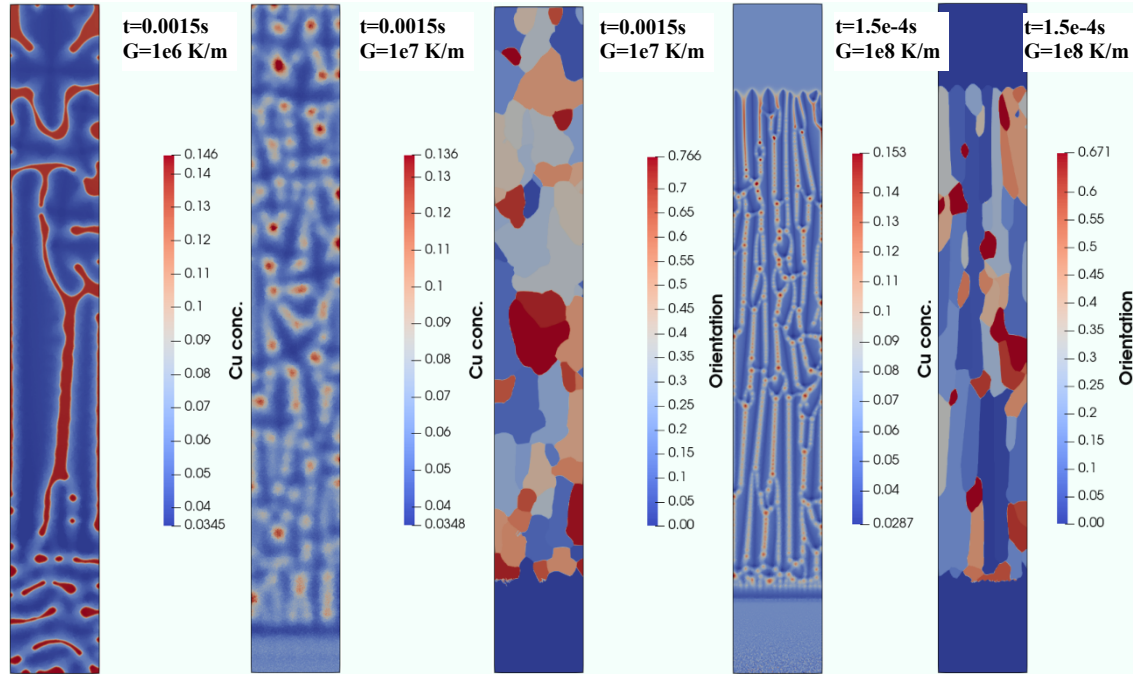


Figure 25. Bulk nucleation in the liquid for Ti-1e-5Nb-0.06Cu alloy for $V = 0.08$ m/s at various G values.

A systematic comparison of the effect of Nb on nucleation and CET was investigated using larger simulation domains, with fixed G and R , at $G = 3.2e5$ K/m and $R = 0.029$ m/s. The simulations were performed in a simulation domain of 2000×1500 mesh points with a moving domain in the build direction. The nucleation parameters used were $I_0 = 10^{30}$ m³/s and $f(\theta) = 0.006$. The simulations were performed for three different levels of Nb, 1.e-5, 0.1, and 0.2, all with 0.06Cu. Since the nucleation parameters and G and R were kept constant, the simulations provide a direct comparison of the effect of Nb content on the nucleation kinetics and microstructure evolution. In all of the simulations, the initial temperature of the liquid at the liquid-substrate interface was equal to the corresponding liquidus temperatures of the alloy.

Figure 26 shows the temporal evolution of the structure for Ti-1e-5Nb-0.06Cu alloy. Liquid nucleation in this alloy occurs after some extent of destabilization of the initially flat interface between the liquid and the substrate. Bottom left and bottom right figures in Figure 26 show the soft impingement of the columnar grains emanating from the substrate and the bulk nucleated grains, that stops further advancement of the columnar grains. Comparing Figure 27 (left) with Figure 26 (bottom right) we can see that the average size of the equiaxed dendrites is smaller in the 0.1Nb alloy compared to the 1e-5Nb alloy. Also, by comparing Figure 26 (top left) with Figure 27 (right), we can see that the nucleation is promoted at a significantly earlier time for the 0.2Nb alloy compared to the 1.e-5Nb alloy.

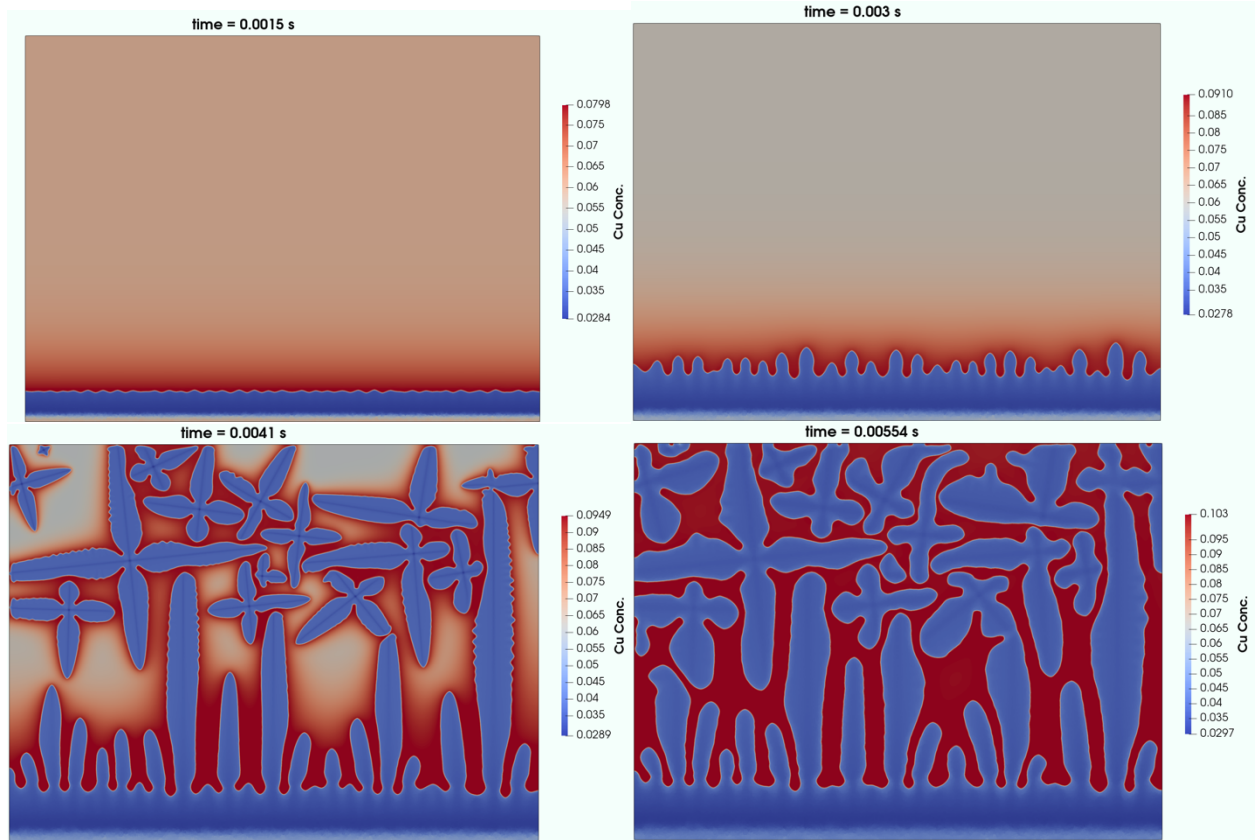


Figure 26. Temporal evolution of the solidification microstructure for Ti-1.e-5Nb-0.06Cu alloy showing liquid nucleation and the formation of equiaxed grains.

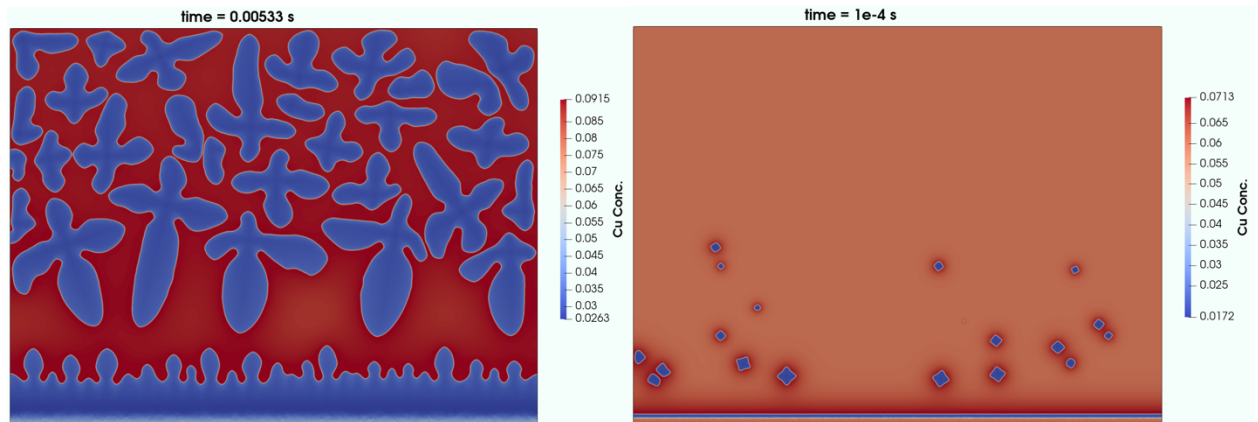


Figure 27. Solidification microstructure of Ti-0.1Nb-0.06Cu (left) and microstructure at the beginning of nucleation for Ti-0.2Nb-0.06Cu (right).

Finally, the time varying $G(t)$ and $R(t)$ were used to drive the solidification in the three Nb-containing ternary alloys by systematically varying the nucleation parameters.

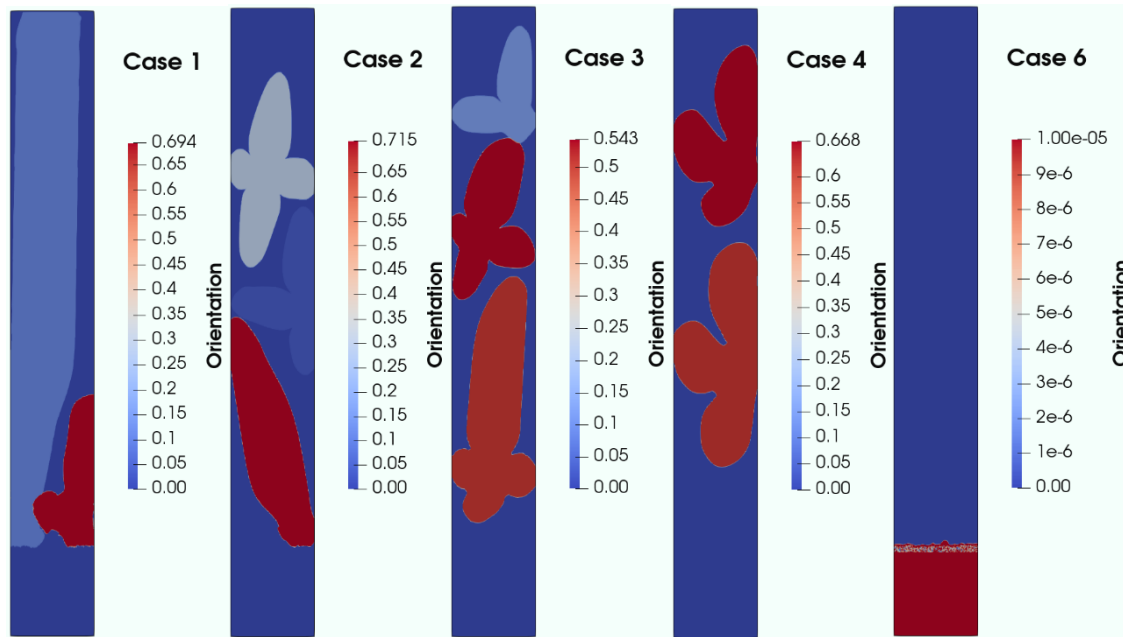


Figure 28. Effect of nucleation parameters on bulk nucleation in Ti-1e-5Nb-0.06Cu alloys.

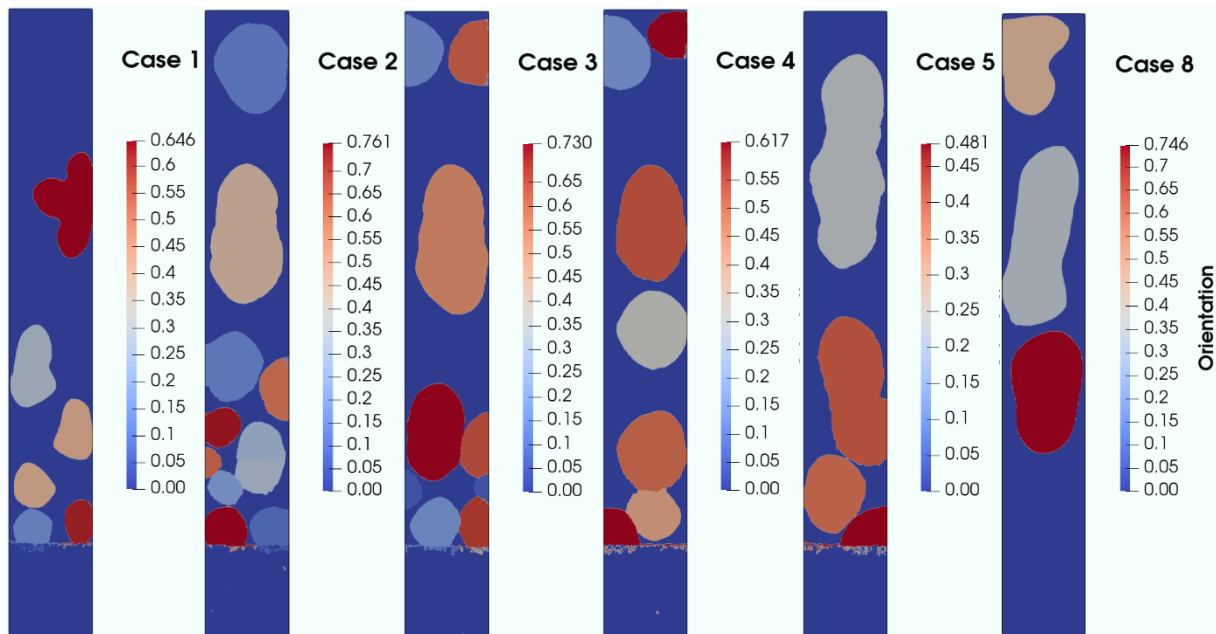


Figure 29. Effect of nucleation parameters on bulk nucleation Ti-0.2Nb-0.06Cu alloy.

The nucleation parameters used in the various cases shown above are listed in Table 3. For the 1.e-5Nb alloy, bulk nucleation fails to occur when $f(\theta)$ increases above 0.006, while for the 0.2Nb alloy, bulk nucleation was observed for all cases studied, showing the effect of Nb in decreasing the activation energy for nucleation.

Table 3. Nucleation parameters used in the parametric study

Case	$I_0 \text{ (m}^{-3}\text{s}^{-1}\text{)}$	$f(\theta)$
1	10^{30}	0.006
2	10^{30}	0.005
3	10^{30}	0.004
4	10^{30}	0.003
5	10^{30}	0.007
6	10^{30}	0.008
7	10^{30}	0.009
8	10^{30}	0.01

4.4.1 Summary Discussion of phase field simulations of CET

MEUMAPPS-SL simulations of CET in Ti-Cu and Ti-Nb-Cu ternary under AM thermal conditions captured several interesting aspects of the phenomenon that are quite distinctly different from analytical models based on the assumption of steady state solidification. Based on nucleation parameters representative of homogeneous nucleation, CET could never be initiated for the G and R conditions characteristic of AM. Epitaxial growth occurred until a steady state was obtained with the dendrite tip velocity, V , approaching the imposed solidification rate, R . For the heterogeneous nucleation conditions, increasing the wetting angle above a certain limit (increasing $f(\theta)$) led to the elongation of the nucleated dendrites. The only conditions under which the nucleated grains remained equiaxed upon growing was when the wetting angle was decreased below a critical value. Since the AM experiments do produce equiaxed dendrites, it is reasonable to assume that the nucleation conditions used in the simulations are close to what is observed experimentally. The thermodynamically consistent nucleation model that was implemented in MEUMAPPS-SL was shown to discriminate the effects of alloy chemistry, the degree of heterogeneity, and the effect of thermal parameters on the nucleation in the bulk liquid ahead of the epitaxially solidifying columnar front, and the formation of CET during solidification of Ti-Cu binary and Ti-Nb-Cu ternary alloys. The simulation results indicate that Nb is a beneficial ternary addition to Ti-Cu alloys to promote the CET even further during rapid solidification to achieve fine equiaxed grains. The use of the thermodynamically consistent nucleation model and full integration of the nucleation model with alloy thermodynamics has resulted in reducing the uncertainties associated with the simulation of CET under AM conditions. Although phase field simulations of CET has remained an active area of research, most of the previous effort has focused on simple assumptions of the nucleation undercooling and artificial “placement of nuclei” in the bulk liquid. The current simulations used a probabilistic nucleation model coupled with classical nucleation theory to calculate the nucleation probability based on the local thermodynamic driving force in the liquid.

For the Ti-Cu binary alloy, the equiaxed grain size that could be obtained by varying the heterogeneous nucleation parameters remained somewhat constant around $2\mu\text{m}$ for the cases studied. According to the interdependence theory [2], reducing the potency of the heterogeneous nuclei should lead to an increase in grain size. However, in the current simulations, reducing the potency leads to either complete absence of nucleation or in the elongation of nuclei. Therefore, the experimentally observed grain size of about 10-20 μm could not be obtained in the simulations. In the current simulations, the main parameter that was changed was $f(\theta)$. Thermodynamic drive force was changed mainly through the Cu content by considering alloys with three levels of Cu. It is possible that the 10-20 μm size of the equiaxed grains measured in AM processed Ti-Cu alloy is after significant thermal aging of the as-cast grains due to the multiple heating cycles associated with the AM process. Future work is required in order to test this hypothesis.

The current simulations indicate that the total undercooling in the liquid is composed of two main contributions – constitutional undercooling and thermal undercooling. All analytical models of CET assume that the moving s-l interface at the dendrite tip is under both thermal and chemical equilibrium. Thermal equilibrium implies that the rate of movement of the temperature isotherms due to imposed cooling rate is the same as the rate of movement of the s-l interface, after a certain steady-state undercooling is reached at the dendrite tip. After this condition is reached, the solute distribution in the liquid ahead of the s-l interface also reaches a chemical equilibrium, so that the concentration profile in the liquid becomes time-invariant. However, when an external cooling rate $G(t) \times R(t)$ is imposed on the system, interface between the substrate and liquid is not under thermal equilibrium initially because the isotherms move at a rate greater than the rate of solidification of the s-l interface, as illustrated in Figure 15. The total undercooling at which nucleation occurs is now driven by the magnitudes of the nonequilibrium thermal undercooling and nonequilibrium constitutional undercooling as represented in Figure 15.

Finally, in all of the above simulations, there is an uncertainty with regard to the initial dynamics of the temperature and solute fields because, the thermal field and the solute field due to solidification are not directly coupled to include the latent heat of solidification. In the binary Ti-Cu simulations, the initial evolution of the s-l interface was handled in the following manner. The temperature at the initial interface between the substrate and the solid was undercooled with respect to the liquid, and the temperature gradient in the solid was artificially increased, in order to minimize the extent of melting of the substrate and to quickly achieve solidification in the build direction. In later simulations of Ti-Nb-Cu ternary alloys, the interface was handled in the following manner. The initial temperature at the substrate-liquid interface was set equal to the liquidus temperature of the alloy with the average composition, and the temperature gradients in the solid and liquid were assumed to be the same. This resulted in significant initial melting of the substrate-melt interface since the substrate also had the same composition (nominal alloy composition) as the liquid. The code was modified to allow translation of the domain in the downward direction during the melting stage so that the interface does not go below the bottom edge of the simulation domain. A question that arises is whether the two drastically different approaches will lead to differences in the prediction of the total nucleation undercooling, and therefore, produce different solidification microstructures. In order to check this issue, the simulations shown in Figure 17 for the binary Ti-0.06Cu binary using time variant $G(t)$ and $R(t)$ and the old interface approach were compared against the Ti-1.e-5Nb-0.06Cu ternary using the new interface approach.

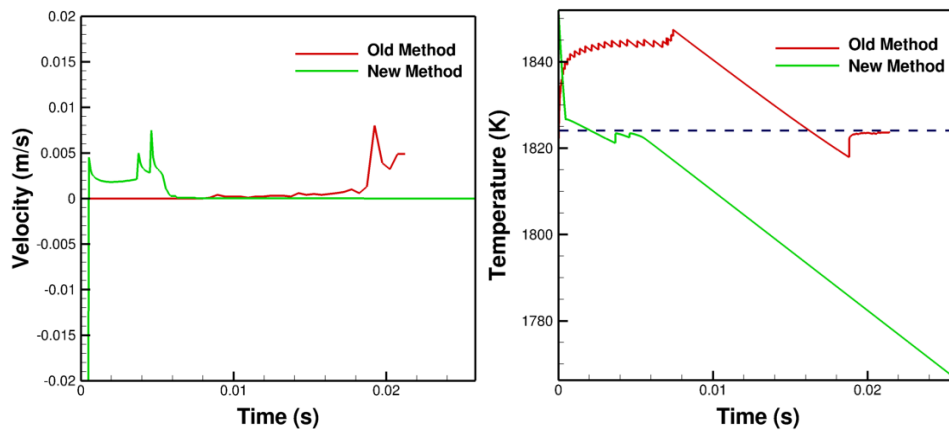


Figure 31. Comparison of the temporal evolution of interface velocity (left) and temperature (right) using two different approaches for initial substrate-liquid interface dynamics.

The temporal evolution of the s-l interface temperature and velocity obtained using the two approaches are shown in Figure 31. It can be seen from Figure 31, that in both approaches the temperature at which the nucleation was triggered in the liquid is roughly the same. Therefore, we can conclude that the predictions of CET using the two approaches should be consistent. However, the new approach is more consistent with the thermal conditions occurring in the melt pool solidification in that the imposed temperature gradient in the solid is more realistic than in the old approach.

Overall, MEUMAPPS-SL simulations of CET are quite promising and should be able to provide useful guidance to the industry in developing and testing novel Ti alloy compositions for AM that could potentially replace the wrought Ti alloys that are used with potential savings in energy and cost.

4.5 AM EXPERIMENTS AND CHARACTERIZATION AT RTRC

RTRC performed AM experiments using a powder laser directed energy deposition (L-DED) process. A 91% CP Ti / 9% Cu powder blend was used as the powder base to produce different Ti/Cu alloys using the DED process. Four nominal compositions of 92.19% CP-Ti / 7.81% Cu alloy, 93.4% CPTi / 6.6% Cu alloy, 94.6% CPTi / 5.4% Cu alloy, and 97% CPTi / 3% Cu alloy were investigated. Due to unavailability of suppliers, the originally planned mechanical alloying to produce 91%Ti / 9% Cu was substituted with blended powder which posed some issues during the DED process. The final objective of the experimental effort was to develop additively manufactured titanium–copper alloys (Figure 30) to form fully equiaxed β -phase titanium grains and prove the concept of generating an ultrafine eutectoid microstructure as the copper % in the Ti/Cu alloy increases. The selected alloy compositions are indicated in the Ti-Cu phase diagram shown in Figure 30.

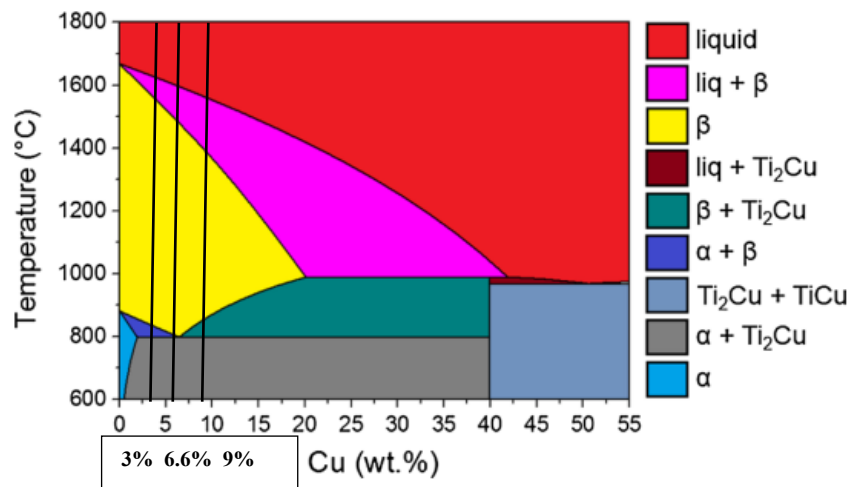


Figure 30. Portion of the Ti/Cu phase diagram [19] indicating the selected compositions for L-DED.

The cross sections of the Ti and Cu used for blending are shown in Figure 31. The materials used to make the Ti/Cu alloys are pure titanium powder and blended 91%Ti-9%Cu powders by weight. The particle size is the same to facilitate the melting of the blended powder with pure titanium powder. The powders were spherical with some satellites and displayed a satisfactory flowability into the nozzle with respect to the process criterion. The materials were deposited onto a 75 mm x 150 mm x 12.7 mm CP Ti substrate.

Ti-Cu Powders

- Both Powder species are spherical and appear similar
 - Difference in atomic number makes the Cu powders a little brighter than Ti with back-scatter detector
- Blue = Ti
- Green = Cu
- Lanthanum detected in powders – La peak is near Ti $\text{K}\alpha$ peak so might be a misidentification

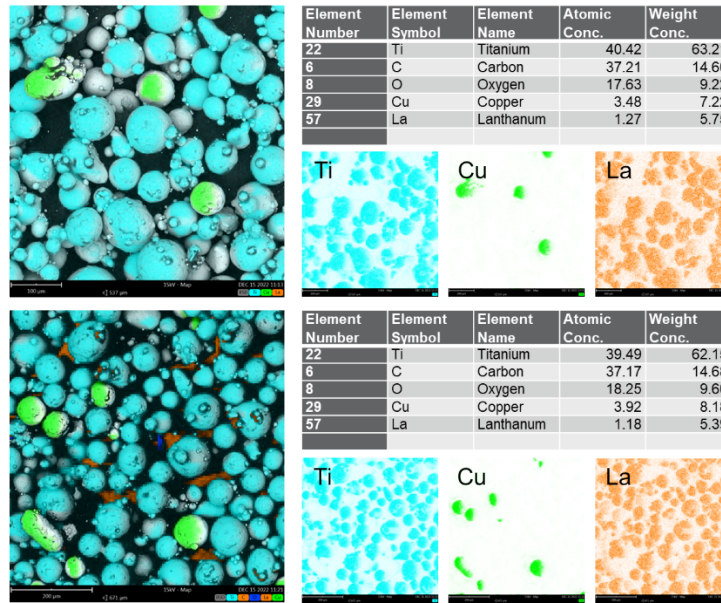


Figure 31. Optical images of the cross-section of raw powders. Blue is image of the titanium powder and green is image of copper powder. The powders are spherical, between 45 μm to 105 μm in diameter.

The samples were fabricated using Optomec Laser Engineered Net Shaping (LENS) machine with powder deposition AM process referred to L-DED process. The LENS machine is equipped with 4-Tip nozzle. A 2 kW IPG Fiber Laser source was used with a focal point position at 12.5 mm. The energy distribution of the laser beam is selectable through optics that allows adjustment of laser spot size, and the selection of either Gaussian or top-hat laser power distribution. Gaussian laser power distribution is used and the diameter of the beam at the focus point is 1.8 mm. Due to the high affinity of Ti alloy with oxygen, manufacturing processes were carried out under argon gas. A gas purification system allows to maintain O_2 level below 20 ppm and H_2O level below 50 ppm. Depending on the chemical composition of the deposit, the process parameters were adjusted. Laser power was adjusted in the range of 800 to 1200 W, travel speed was set in the range of 800 to 1270 mm/min, powder feed rate was adjusted in the range of 0 to 20 g/min, and layer height step was set in the range of 0.38 to 0.5 mm. In the case of making different alloying of Ti/Cu, a differential injection was used to enable the manufacturing of in situ Ti/Cu alloys. For this purpose, differential injection was composed of two powder feeders, each one containing a different powder (blended Ti/Cu or CP Ti), alloying to control the variation in chemical composition. The powders are then injected into a homogenization chamber where the powders are mixing before being injected into the nozzle and then deposited onto the baseplate.

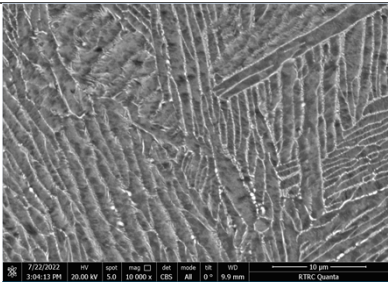
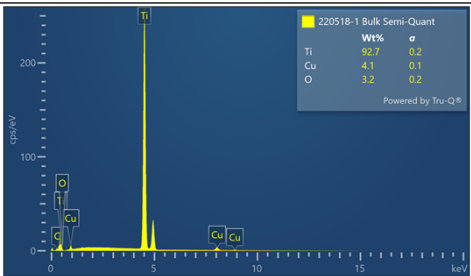
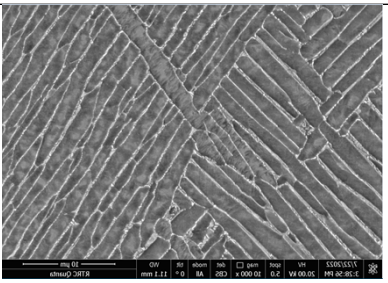
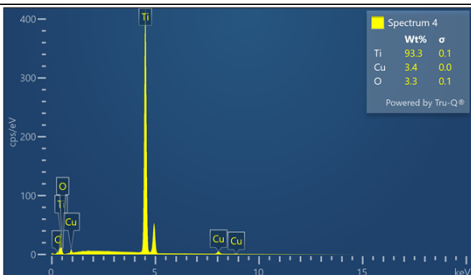
Before manufacturing the tensile samples, single-layer samples were deposited to define defects free process parameters. The samples were tested optically to ensure that there is no balling, lack-of-fusion, and discontinuous defects in the weld bead. The optimized laser metal deposition parameters for the studied alloys are laser power, 960 W; scanning speed, 800 mm/min; laser spot size, 1.8 mm; powder flow rate, 2.8 rpm (2.38 g/min); hatch distance, 1.05 mm; and shielding gas (argon) flow, 5 l/min. The processing parameters were kept the same for all Ti-xCu alloys. Many rectangular specimens of 25.4 x 15.24 x 12.7 mm were built on a commercially pure titanium plate with different compositions (3.0 wt%, 5.4wt%, 6.6 wt%, 7.8 wt% and 9wt% copper). The laser scanning route for laser metal deposition was a raster pattern with an increment of 90° between each layer, and the delay time between two subsequent layers was 30 s. For comparison, a Ti6Al4V specimen was additively manufactured using the same

parameters. Tensile samples were made from blended Ti/Cu powders instead of alloying the samples layer by layer. 12 mm diameter cylinders with a length of 85 mm were deposited on a commercial CP Ti substrate. The samples were then machined to standard tensile samples. The loading direction of tensile samples is perpendicular to the laser metal deposition building direction.

4.5.1 Chemical Compositions

The chemical composition of the as-printed samples was determined by EDS (Electron Dispersive X-ray spectroscopy), as shown in Table 1. The results indicate that some copper was evaporated as its boiling point is 2,560°C, much lower than that of titanium (3,285°C) [20], and that titanium has been oxidized.

Table 4. EDS data indicating the percentage of Ti/Cu/O elements in the alloy

Ti / Cu alloy composition	backscattered electrons (BSE) microstructure	EDS												
92.7% Ti / 7.3% Cu		 <table border="1"> <thead> <tr> <th>Element</th> <th>Wt%</th> <th>σ</th> </tr> </thead> <tbody> <tr> <td>Ti</td> <td>92.7</td> <td>0.2</td> </tr> <tr> <td>Cu</td> <td>4.1</td> <td>0.1</td> </tr> <tr> <td>O</td> <td>3.2</td> <td>0.2</td> </tr> </tbody> </table>	Element	Wt%	σ	Ti	92.7	0.2	Cu	4.1	0.1	O	3.2	0.2
Element	Wt%	σ												
Ti	92.7	0.2												
Cu	4.1	0.1												
O	3.2	0.2												
93.3% Ti / 6.7% Cu		 <table border="1"> <thead> <tr> <th>Element</th> <th>Wt%</th> <th>σ</th> </tr> </thead> <tbody> <tr> <td>Ti</td> <td>93.3</td> <td>0.1</td> </tr> <tr> <td>Cu</td> <td>3.4</td> <td>0.0</td> </tr> <tr> <td>O</td> <td>3.3</td> <td>0.1</td> </tr> </tbody> </table>	Element	Wt%	σ	Ti	93.3	0.1	Cu	3.4	0.0	O	3.3	0.1
Element	Wt%	σ												
Ti	93.3	0.1												
Cu	3.4	0.0												
O	3.3	0.1												

The images are determined from the center of the deposited samples. The pseudo-bulk EDS measurement was taken for reference between the samples. The relative amount of copper follows the correct trend, but these measurements showed less copper than target. These results indicated that alloying the Ti/Cu using the DED process is not as accurate as expected because of the evaporation of copper and the affinity of the Ti alloy.

4.5.2 Microstructures

The microstructures obtained using DED are shown in Figures 32 and 33. The results obtained are very close to those obtained in reference [7] for the Ti-3.5Cu. The grain refinement however did not match those obtained in reference [7]. The optical micrographs of the as-printed Ti-7.8Cu specimen showed some equiaxed prior-β grains without any noticeable cracks or porosity. The as-printed specimen also shows homogenous copper content along the building direction; however, the grain size was larger in the

middle layers and refined at the top and bottom layer of the specimen. The prior- β grains have a bimodal distribution with an average grain size of 15 to 20 μm , compared with coarse columnar grains microstructure of as-printed Ti6Al4V alloy observed always in DED deposition. The addition of copper was expected to fully convert the columnar grains to equiaxed grains and refined the prior- β grains by two orders of magnitude. Unfortunately, it seems that the occurrence of this phenomenon depends to a great extent on the condition of the powder blend and capability of the machine to in situ alloy the material during deposition.

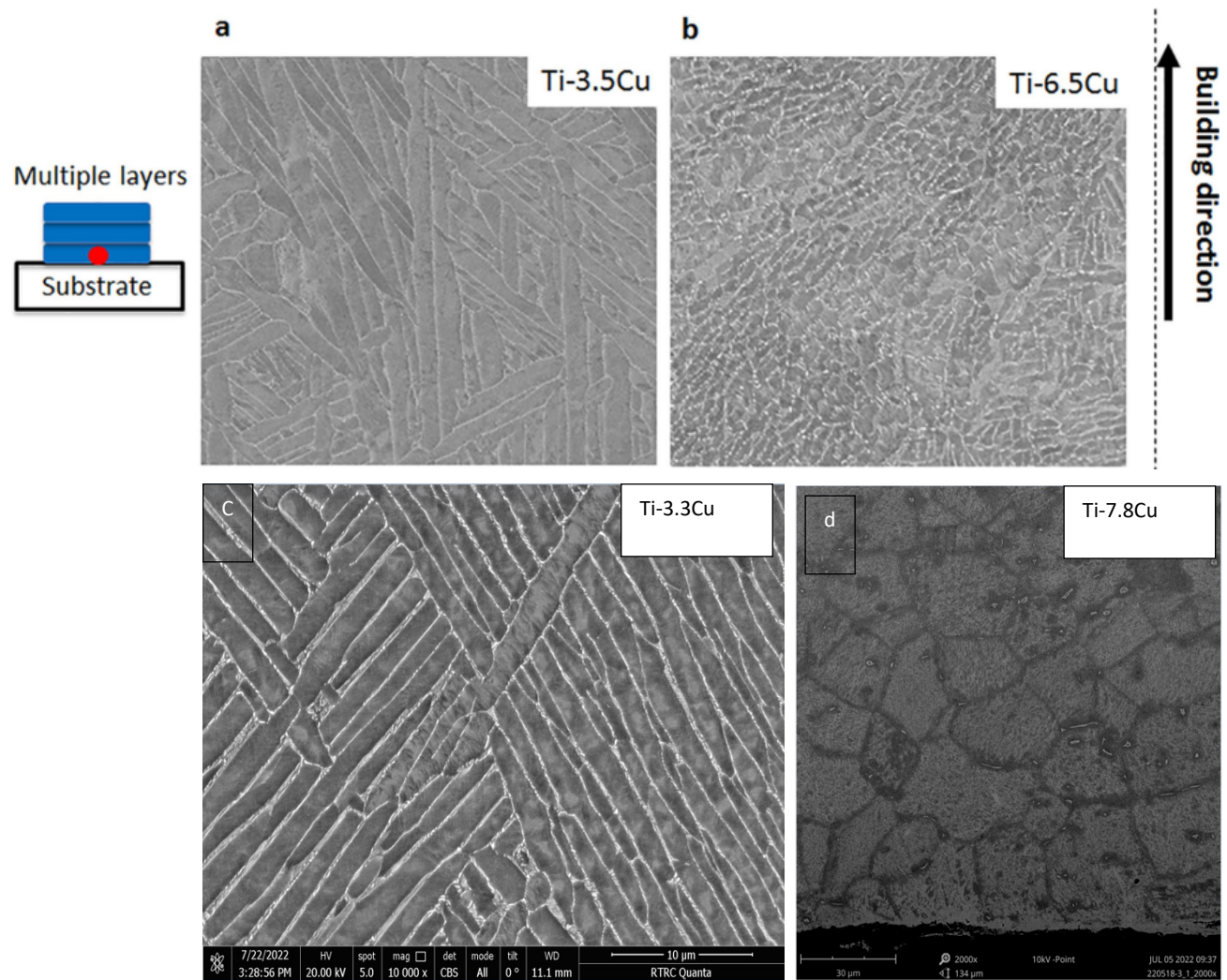


Figure 32. BSE images. a and b are BSE images of as-printed specimens showing the fine α phases when multiple layers were deposited, for Ti-3.5Cu (a) and Ti-6.5Cu (b) [7]; c and d results are obtained using DED at RTRC. When the copper content in the alloy is 3-4% the grain structure produced is the same as in a and b, however with the increase in the copper content grain refinement occurs not across all the layers, but only in the first and last layers.

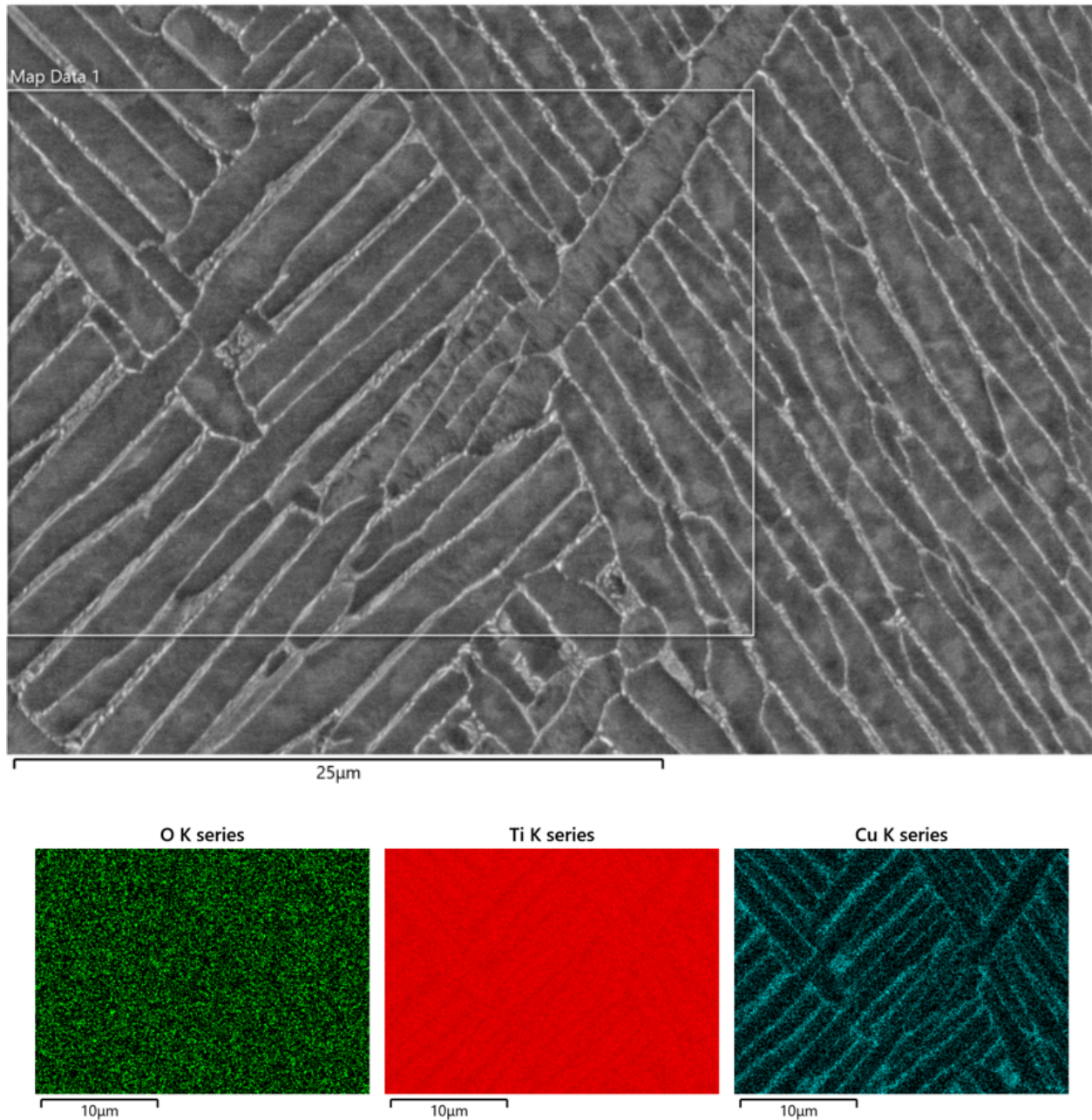


Figure 33. Transmission electron microscopy characterization of as-printed Ti–6.7Cu alloy. a, Bright-field image showing the eutectoid lamellar structure. b–d, X-ray energy dispersive spectroscopy (XEDS) mapping on a section of the eutectoid lamellar structure: Oxygen elemental map (b), titanium elemental map (c) and copper elemental map (d). XEDS point analyses show that the copper contents in the lamellar structure are 3.3 wt% in α -phase titanium.

4.5.3 Mechanical Testing

Tensile tests with sub sized ASTM standard specimens were performed on the as-printed blended alloys and the associated 0.2% offset yield strength (σ_y), ultimate tensile strength, and uniform elongation (ϵ) are summarized in Table 2. Comparing the different Ti/Cu alloys, the

eutectoid lamellae in high copper percentage in the alloy increases the strength, however, it did not increase the strength higher than the Ti64 strength. The main reason is the experimental setup used did not produce a very refined grain structure.

Table 5. Mechanical properties of as-printed Ti–Cu alloys

%Cu in TiCu sample	UTS ksi	YS ksi	Elongation %
9	96.4	95	23
9	96.9	95.6	22
7.8	91.88	91.72	24
7.8	90.07	89.8	25
6.6	88.65	87.64	25
6.6	91.4	90.45	25
5.4	84.8	83.61	29
5.4	84.29	83.31	30
3	85.61	85.09	26
0	64.76	63.74	34
0	63.3	63.1	40
Ti64	138	128	14
CP Ti	62.4	49.3	28

4.5.4 Summary of Experimental Results

The DED experiments posed some issues due to the inability of the blended powders to feed well in the dispensers. The equiaxed grain size obtained in the experiments was higher than what is reported in the recent literature [7], probably due to the differences in the manner in which the initial powder stocks were prepared and used to obtain the different compositions in the DED process. The mechanical test results also did indicate a lower yield stress and a higher ductility compared to the recent literature [7] consistent with the larger grain size obtained. Further optimization of the powder stock and DED process have to be undertaken in order to obtain the lowest possible grain size in a consistent manner.

5. REFERENCES

1. J. H. Martin et al., “3D printing high-strength aluminium alloys,” *Nature*, 549, 2017, pp. 365-369, doi:10.1038/nature23894.
2. D. H. StJohn et al., “The interdependence theory: The relationship between grain formation and nucleant selection,” 59, 2011, pp. 4907-4921.
3. J. Zhang et al., “Fine Equiaxed Beta grains and superior tensile property in Ti-6Al-4V alloy deposited by coaxial electron beam wire feeding additive manufacturing,” *Acta Metallurgica Sinica*, 33, 2020, pp. 1311-1320.

4. R. Shi et al., "Microstructural control in metal laser powder bed additive manufacturing using laser beam shaping strategy," *Acta Materialia*, 184, 2020, pp. 284-305.
 5. C. J. Todaro et al., "Grain structure control during metal 3D printing by high-intensity ultrasound," *Nature Communications*, 11, 2020, article number 142.
 6. M.J. Bermingham et al., "Promoting columnar to equiaxed transition and grain refinement of titanium alloys during additive manufacturing," *Acta Materialia*, 168, 2020, pp. 261-271.
 7. D. Zhang et al., "Additive manufacturing of ultrafine-grained high-strength titanium alloys," *Nature*, 576, 2019, pp. 91-95.
 8. B. Radhakrishnan, et al., "Phase field simulations of microstructure evolution in IN718 using a surrogate Ni-Fe-Nb alloy during laser powder bed fusion," *Metals*, 9, 2019, 14, doi: 10.3390/met9010014.
 9. B. Radhakrishnan, S. Gorti, and Y. Song, "Design of Novel Titanium Based Alloys for Additive Manufacturing using HPC-Aided Large-Scale Phase Field Simulations, Oak Ridge National Laboratory, ALCC, Oak Ridge Leadership Computing Facility (OLCF), 1,250,000 node-hours on Summit.
 10. B. Radhakrishnan, "Development of HPC based phase field simulation tool for modification of alloy morphology to enhance material properties during additive manufacturing (AM) process," NREL HPC Projects, 594554 ASUs on Eagle supercomputer at NREL.
 11. U. R. Kattner, "The Calphad method and its role in material and process development," *Tecnol. Metal. Mater. Miner.*, São Paulo, v. 13, n. 1, p. 3-15, Jan./Mar. 2016.
 12. C. V. Thompson and F. Spaepen, "Homogeneous crystal nucleation in binary metallic melts," *Acta metal.* 31, 2021-2027 (1983).
 13. J. Li et al., "Phase-field simulation of microstructure development involving nucleation and crystallographic orientations in alloy solidification," *Journal of Crystal Growth* 309 (2007) 65-69.
 14. J. P. Simmons, C. Shen, and Y. Wang, "Phase field modeling of simultaneous nucleation and growth by explicitly incorporating nucleation events," *Scripta Materialia* 43 (2000) 935-942.
 15. S.G. Kim, W. T. Kim, and T. Suzuki, "Phase-field model for binary alloys. *Phys. Rev. E* 60 (1999), pp. 7186–7197.
 16. K. Momeni, V. I. Levitas, and J. A. Warren, "The strong Influence of Internal Stresses on the Nucleation of a Nanosized, Deeply Undercooled Melt at a Solid–Solid Phase Interface," *Nano Letters*, 15 (2015) pp. 2298-2303.
 17. J. D. Hunt, "Steady state columnar and equiaxed growth of dendrites and eutectic," *Materials Science and Engineering*, 65, 1984, pp. 75-83.
 18. A. Badillo and C. Beckermann, "Phase-field simulation of the columnar-to-equiaxed transition in alloy solidification," *Acta Materialia*, 54, 2006, 2015-2026.
-

19. K. N. campo et al., “On the selection of Ti-Cu alloys for thixoforming processes: phase diagram and microstructural evolution,” 50 (2015) 8007-8017.
20. E. A. Brandon and G. B. Brooks, Smithells Metals Reference Book 7th Edn. (Butterworth-Heinemann, 1992).

ACKNOWLEDGMENTS

This research was supported by the High-Performance Computing for Manufacturing (HPC4Mfg) program sponsored by the Advanced Manufacturing Office of the U.S. Department of Energy (DOE). Development of the MEUMAPPS-SL PF code was partially funded by the Exascale Computing Project (17-SC-20-SC), a collaborative effort of the U.S. DOE Office of Science and the National Nuclear Security Administration. This research used resources of the Oak Ridge Leadership Computing Facility, which is a DOE Office of Science User Facility supported under contract DE-AC05-00OR22725, as well as the Eagle supercomputer at NREL. Research performed at the Oak Ridge National Laboratory (ORNL), managed by UT-Battelle, LLC, under Contract No. DE-AC05-00OR22725 for the U.S. DOE.